1-23-2020

Calibration Transients In LIGO Detectors

Thomas Daniel Abbott

CALIBRATION TRANSIENTS IN LIGO DETECTORS

A Dissertation

Submitted to the Graduate Faculty of the
Louisiana State University and
Agricultural and Mechanical College
in partial fulfillment of the
requirements for the degree of
Doctor of Philosophy

in

The Department of Physics and Astronomy

by
Thomas Daniel Abbott
B.S., California State University, Fullerton 2010
M.S., California State University, Fullerton 2012
May 2020

PREFACE

Interferometric gravitational wave detection is a multinational, interdisciplinary undertaking that thrives on the skills of thousands of people from diverse backgrounds. Scientists, engineers, computer programmers, teachers, students, citizen scientists, etc. all are vital components to this field's ability to make cutting-edge contributions to human knowledge through scientific inquiry, and to contribute to the well-being of the greater community through educational outreach programs which enrich the public with enthusiasm for the pursuit of discovery.

The research presented in this thesis was carried out within the LIGO Scientific Collaboration (LSC). Although much of this work stemmed from discussion and collaboration with LSC members, this dissertation has not been reviewed by the collaboration. Opinions expressed here are my own and not necessarily those of the LSC.

ACKNOWLEDGMENTS

I would like to thank Gabriela González for being an amazing advisor, for her guidance and patience, for making the LSU experimental gravity group a welcoming and fulfilling research group to work in, and for giving me the awesome opportunity to work on my PhD doing research for LIGO during the first-ever direct measurement of gravitational waves!

I'd also like to thank Joshua Smith for introducing me to LIGO and taking me in as a Masters student. I really had a great time working in his lab and learning all about the LIGO instrument and detector characterization. The experience changed my life for the better.

Thank you to Rick Savage for giving me the opportunity to work with his team while the photon calibrator system was being installed. I gained a lot of knowledge about control systems, calibration, and fishing from that experience.

There were countless people who were invaluable to me when learning about LIGO and working on my thesis. Thanks to the instrumental experts such as Anamaria Effler, Stuart Aston, Joe Betzweiser, Adam Mullavey, Shivaraj Kandhasamy, Marie Kasperek (and many more) for answering my questions and throwing some epic nuggets of knowledge my way. Thank you to all the people of the calibration and detector characterization groups for all of their hard work. Thanks to Duncan MacLeod for GWpy and for being awesome, and thanks to his wife, Lucy, for also being awesome and for a copy of "A Simples Life" by Aleksander Orlov, a book which chronicles the life of an extraordinary meerkat. Thanks to Jess McIver for sharing knowledge of the seismic and suspension isolation systems as well as encouraging Adventure Time quotes. Thanks to TJ Massinger for being such a complete bad-ass and for giving an excellent ALS talk that really helped further my understanding of how the interferometer locks. Thank you to Evan Goetz for your help with calibration uncertainty. Thank you so much to Alex Urban and Guillermo Valdés for being extremely helpful and answering so many of my day-to-day questions.

Thank you to Andy and Sam for keeping me company at all ungodly hours of the night while I was working on my thesis. Thank you to my mom, Simone, and dad, Tim, for conjuring me into existence! Thank you to Joni for your continued encouragement and for all the fun times. Thank you to Brodie for being a pal and always having my back. Thank you to Eric for all the frivolous trips to the Dollar Tree and for being a great uncle.

My last acknowledgement I save for my grandparents, Bonnie and Leroy. I am deeply thankful for all the love and support you have given me my whole life. Without you this dissertation would not have been written.

TABLE OF CONTENTS

LIST OF TABLES

LIST OF FIGURES

ABSTRACT

This dissertation describes a novel method of analyzing fluctuations in the time-dependent calibration models of the LIGO interferometers to estimate their effect on strain reconstruction for gravitational-wave detections. The time-dependence of the calibration model of each detector is tracked with a set of parameters which are continuously measured while the interferometers are operating. These parameters track slow variations in the sensing function of the detectors as well as the actuators that hold the detectors in an operational state. The time-dependent parameter data during the second observation run (O2 [November 30, 2016 16:00 UTC to August 25, 2017 22:00:00 UTC]) and the first epoch of the third observation run (O3a [April 1, 2019 15:00 UTC to October 1, 2019 15:00 UTC]) were combed for significant fluctuations. A modified z-score was used as a standardized metric to identify and sort time segments which correspond to noise transients in the time-dependent calibration parameters for both detectors. The results of our search through O2 data from the LIGO Hanford Observatory (LHO) identified a set of relatively few noise transients all with negligible statistical significance, demonstrating that the behavior of the time-dependent calibration parameters at LHO were largely consistent with Gaussian noise on 30-minute or less time scales. Our search through O2 data from the LIGO Livingston Observatory (LLO) showed similar results for the parameters that track variations in actuation. Likewise, the sensing function parameters were mostly consistent with Gaussian noise as well; however, our search identified a small set of statistically significant noise transients. None of which were coincident with gravitational-wave signals, and the most significant of which were estimated to momentarily increase the strain reconstruction 1σ uncertainty from 1% to 3% in the regime of the interferometers' most sensitive frequency band (150 Hz). Like the O2 results, analysis of O3a data revealed that all the time-dependent calibration parameters at each detector were mostly consistent with Gaussian noise on 30-minute or less time scales. Our results demonstrate that overall, the time-dependent calibration parameters experienced very few significant fluctuations throughout O2 and O3a, and even largest transient we found would have minimal impact on gravitational-wave measurements.

CHAPTER 1. INTRODUCTION

The Laser Interferometric Gravitational-wave Observatory (LIGO) consist of two complex interferometric detectors separated by 3000km that measure fluctuations in space-time caused by cataclysmic astrophysical events deep in the cosmos. Both detectors are located in the United States; one is in Hanford, Washington, while the other resides in Livingston, Louisiana. The LIGO detectors consist of a Michelson interferometer equipped with two 4-km Fabry-Perot cavities, a power-recycling cavity in the symmetric port to increase the input laser power, a signal-recycling cavity in the anti-symmetric port to tune the detector response bandwidth, and a myriad of other systems which all work in concert to allow LIGO to measure differences in arm lengths down to the order of 10^{-20}m/$\sqrt{\text{Hz}}$ at 150Hz [1] at the time of writing.

The construction of the LIGO sites was finished in the late 1990s, and the first observations began in 2005 and continued intermittently until 2010 [1]. In their initial state, the interferometers were sensitive to arm length fluctuations down to the order of 10^{-18}m/$\sqrt{\text{Hz}}$ at 150Hz, so the chances of making a direct detection of gravitational-waves were slim, and indeed one was not made in that time frame. However, this time was not wasted as the lack of observation contributed to the upper-limits of astrophysical rate estimates, and allowed the project to expand the understanding of large-scale intereferometers, paving the way for the next generation of gravitational-wave detectors.

From 2010 to 2015, the LIGO interferometers were shutdown and underwent various upgrades (e.g. improved seismic isolation systems) which lowered the noise floor by a factor of approximately 10^{-3} at 150Hz, this second generation version of LIGO is deemed Advanced LIGO. On September 14, 2015, technically 4 days before the start of the beginning of Advanced LIGO's first observation run (O1), the LIGO observatories achieved the world's first direct detection of gravitational waves. A clear signal which featured a frequency and amplitude evolution consistent with the merger of two compact stellar objects. On February 11, 2016, after months of careful investigation, the LIGO Scientific Collaboration announced that the signal was caused by the inspiral and merger of two

intermediate-mass black holes approximately 1.3 billion light-years away [2]. O1 would last until January 12, 2016, and two more binary black hole merger signals would be detected.

Following the success of O1, the LIGO detectors shutdown operations to undergo upgrades for nearly 11 months before starting the second observation run (O2) on November 30th, 2016. This time the Italian detector, Virgo, had finished undergoing upgrades and joined LIGO on August 1, 2017, adding to the world-wide network of gravitational-wave detectors. The LIGO-Virgo Collaboration made eight new detections during O2. Most notably, on August 17, 2017, the first gravitational-wave signal from the merger of two neutron stars was detected in both LIGO detectors as well as the Virgo detector. In addition, this event was corroborated by independent electromagnetic observations. For instance, the short gamma-ray burst (GRB 170817A) from the neutron-star collision was independently detected by the *Fermi* Gamma-ray Burst Monitor [3], ushering in the beginning of multimessenger astronomy [4].

Since then the LIGO and Virgo detectors have achieved even greater sensitivity, and completed the first phase of the 3rd observation run (O3a), spanning from April 1, 2019 to October 1, 2019. During this time thirty-two more gravitational-wave signals have been detected, including more binary neutron star mergers, as well as signals from the collision of a black hole and a neutron star. The detection rate of O3 so far has been considerably higher than during previous observation runs, and it is expected to increase even more once the Japanese gravitational-wave detector is operational in late 2019.

Contemporary gravitational-wave detectors use laser interferometry to measure extremely small fluctuations in local space-time which cause fluctuations in laser power which are recorded as an electronic output signal. The output signal must be calibrated into astrophysical units by accounting for the optomechanical response of the interferometer in order to make statements about a possible detected gravitational wave. Since the interferometer response is expected to vary slightly over the duration of an observation run, time-dependent components were added to the Advanced LIGO calibration model and tracked to compensate.

This dissertation will focus on the calibration of the LIGO detectors, and the effect that large noise transients in the detector can have on the accuracy of minute-scale time-dependent corrections to the calibration. Chapter 2 gives a brief introduction of gravitational waves. Chapter 3 discusses basic relevant information regarding interferometry and calibration of LIGO detectors. Chapter 4 discusses the photon calibrator (PCAL) subsystem of Advanced LIGO, specifically on a photometric estimation of the uncertainty introduced via test mass rotations induced by beam misalignment of the PCAL beams. Chapter 5 discusses a statistical search for significant fluctuations in parameters used to track time-dependent parameters during the 2nd observation run of Advanced LIGO, which were not previously found by vetoes, the results of that search, and an estimation of the effect of the worst-case offenders on the calibration uncertainty of the instruments. Chapter 6 discusses a similar, preliminary analysis performed on the first 6 months of the 3rd observation run (O3a). Chapter 7 concludes our study.

CHAPTER 2. GENERAL RELATIVITY

2.1. Gravitational Radiation

Isaac Newton's Theory of Universal Gravitation describes gravitation as an attractive force between two objects with mass. The magnitude of the force is proportional to the product of their masses and inversely proportional to the square of their spatial separation. It is an extremely accurate model when it comes to ordinary gravity on the surface of Earth and even when it comes to predicting most celestial mechanics; however, it is ultimately flawed in regimes of strong gravity, and it proposes a gravitational force that propagates instantaneously over any distance, which is at odds with our knowledge that the speed limit of information through space has a finite, frame-invariant value, $c = 299\,729\,458\,\mathrm{m/s}$.

Albert Einstein's theories of Special and General Relativity propose a geometrical model of space-time which explains this phenomenon and models gravitation as the manifestation of physics in a curved space-time, and a result of this theory is that disturbances in the gravitational field do not propagate instantaneously. They propagate at c, and these travelling disturbances in the gravitational field are known as *gravitational waves*.

In order to concisely invoke the mathematical logic that motivates the existence gravitational waves, we start with the Einstein Field Equations (EFE) [5].

$$R_{\mu\nu} - \frac{1}{2}Rg_{\mu\nu} + \Lambda g_{\mu\nu} = \frac{8\pi G}{c^4}T_{\mu\nu} \tag{2.1}$$

This tensor equation relates the curvature of space-time to energy-momentum density. On the left-hand side, the Ricci curvature tensor and its trace, R, known as the Ricci scalar, $R_{\mu\nu}$, correspond to the curvature of a local space-time. The Ricci tensor is calculated from non-linear combinations of the derivatives of the metric tensor, $g_{\mu\nu}$, which carries information about the structure of space-time and causality. Finally, the cosmological constant, Λ, is a correction factor which allows for an expanding universe.

On the right-hand side, there is one term with a coefficient that includes the Newtonian gravitational constant, G, and the speed of light, c. The stress-energy tensor, $T_{\mu\nu}$, contains information about the energy/momentum density of the gravitational system. The solutions to the EFE can be used to determine the evolution of a gravitational system.

The scope of this dissertation will focus on gravitational radiation observed sufficiently far away from the source to warrant the consideration of a small perturbation $h_{\mu\nu}$ to the Minkowski metric $\eta_{\mu\nu}$ in the weak-field limit and *Transverse-traceless gauge* (equation 2.2), in which case the EFE reduce to leading order to a linear tensor equation (equation 2.3) [6].

$$g_{\mu\nu} = \eta_{\mu\nu} + h_{\mu\nu} \tag{2.2}$$

$$\left(\nabla^2 - \frac{1}{c^2}\frac{\partial^2}{\partial t^2}\right)h_{\mu\nu} = 0 \tag{2.3}$$

The simplified form may be recognized as the equation of a wave which describes the perturbation propagating through space-time at the speed of light. The mathematical tensor object which describes with travelling perturbation, $h_{\mu\nu}$, is called the gravitational-wave strain tensor, and its physical manifestation is called the gravitational-wave strain. The strain is what gravitational-wave detectors measure as the perturbation passes through the instrument. Furthermore, in the transverse-traceless gauge, the strain of a gravitational-wave traveling the $+z$ direction may be expressed as

$$h_{\mu\nu} = \begin{bmatrix} 0 & 0 & 0 & 0 \\ 0 & a & b & 0 \\ 0 & b & -a & 0 \\ 0 & 0 & 0 & 0 \end{bmatrix} \tag{2.4}$$

This may also be expressed as a linear sum of two components. $h_{\mu\nu} = ah_+ + bh_\times$, where

$$h_+ = \begin{bmatrix} 0 & 0 & 0 & 0 \\ 0 & 1 & 0 & 0 \\ 0 & 0 & -1 & 0 \\ 0 & 0 & 0 & 0 \end{bmatrix} \tag{2.5}$$

and

$$h_\times = \begin{bmatrix} 0 & 0 & 0 & 0 \\ 0 & 0 & 1 & 0 \\ 0 & 1 & 0 & 0 \\ 0 & 0 & 0 & 0 \end{bmatrix} \tag{2.6}$$

.

Here, h_+ and $h_\times$ form an orthogonal basis for expressing the polarization of a gravitational-wave traveling in the +z direction. The h_+ component will oscillate between stretching space along the x-axis while compressing space along the y-axis and vice-versa (Fig. 2.1), while the $h_\times$ component expresses stretching and compression along perpindicular axes rotated 45° around the z-axis. The polarization of gravitational waves is important to account for as not all signals will be aligned with the arms of the detectors [6].

2.2. Gravitational-wave Sources

General Relativity predicts that any system with a non-vanishing quadrupole moment second-time derivative, will emit gravitational waves. More specifically,

$$h_{\mu\nu} = \frac{2G}{Rc^4} \ddot{I}_{\mu\nu} \tag{2.7}$$

Simply stated, this means that if a system undergoes an asymmetric redistribution of its mass/energy density, gravitational-waves are created. As a counterexample, if an object rotates

6
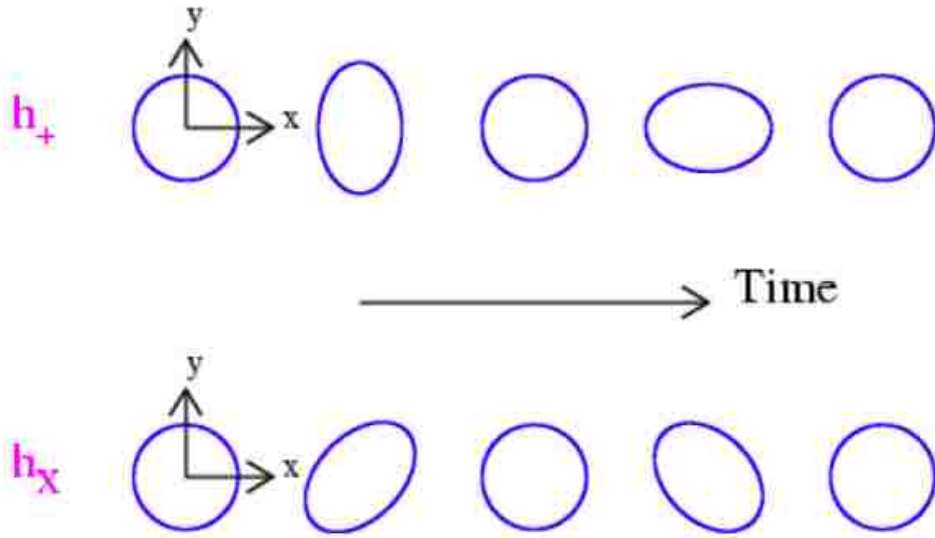
Figure 2.1: An exaggerated illustration of the effect of the different polarization bases of a passing gravitational wave on a ring of test masses [7].

about a symmetric axis (e.g. a spinning top spinning without precession, or a spinning sphere) will not produce gravitational waves. If, however, the object rotates about a non-symmetric axis, gravitational waves are produced. But that does not mean people will detect every ripple in space-time that is created.

The coefficient, $\frac{2G}{c^4} = 1.65 \times 10^{-44}\,\mathrm{s^2/kgm}$, is such an absurdly small quantity that there is currently no feasible way to detect a gravitational-wave signal from everyday occurrences here on Earth. Instead, current terrestrial detectors are sensitive to gravitational wave signals from cataclysmic astrophysical events. These sources can be categorized using two dimensions: duration of signal, and whether a good model exists.

The most prominent well-modeled source of short-duration signals is the *Compact Binary Coalescence* (CBC). In the final moments of binary systems comprised of dense stellar objects (i.e. some combination of neutron stars and/or black holes), these objects will be orbiting each other at relativistic speeds, disturbing space-time enough for detectors on Earth to measure it. CBC signals are well-modeled, so matched-filtering techniques may be employed to find such signals in the data [7].

On the other hand, supernovae are hypothesized to be a promising source of short-duration gravitational wave signals which are not well modeled. An asymmetry in the rapid expulsion of matter and energy from a supernova is expected to produce gravitational waves strong enough to potentially be measured by Earth-based detectors. Since the gravitational-wave signals emitted from a supernova are not yet well understood, matched-filtering methods cannot be used to find burst signals in noisy data. Instead, the data are combed for excess energy coherent in both detectors.

Well-modeled, long-duration signals are also prospective detections. These would be the *continuous-wave* (CW) gravitational-wave signals produced by rapidly spinning neutron stars. Neutron stars are so dense that a small mountain on the surface could produce a signal at a well-defined frequency and phase that may become evident with month-to-year-time-scale integrations of data.

Long-duration, unmodeled signals *(stochastic signals)* are the cumulative gravitational-wave signals from numerous events throughout the universe and those left over from the Big Bang.

CHAPTER 3.   INTERFEROMETRIC GRAVITATIONAL-WAVE DE-TECTORS

3.1.   Interferometry

Albert Einstein had doubts regarding the feasibility of a direct measurement of gravitational waves, but he was not privy to the extremely high-precision measurements made possible with laser interferometry, a discipline of high-precision measurement techniques which is at the heart of modern gravitational-wave detectors. When electromagnetic fields combine, they do so in superposition. That is, if there are multiple sources of an electromagnetic source in a system, the total resulting field is simply the sum of the constituent fields. If the waves are in phase, that is called constructive interference, and the resulting field amplitude will increase. If, however, they are out of phase the waves will cancel each other out in a process called destructive interference. This principle is widely used to make very precise measurements, and furthermore an apparatus that uses interferometry to make measurements is an interferometer. There are many types, each with unique characteristics and uses, but the type of interferometer upon which LIGO is built is called the Michelson interferometer.

Simply put, the Michelson interferometer (Fig. 3.1) consists of a coherent laser source at the symmetric port which shines onto a beam splitter (BS) at the vertex where it is partially transmitted and partially reflected. The transmitted and reflected beams travel down paths, l_x and l_y, respectively. At the end of which, they encounter perfectly reflective mirrors, M_1 and M_2, and are reflected back along the same paths, recombining at the antisymmetric port where its intensity is measured at a photodetector. The intensity of light that the photodetector observes is related to the relative phase of the beams from each path. Since the phase of a light beam depends on its path length, the differential path lengths will determine the intensity of light at the photodetector.

The emitted laser is coherent up until it is split at the BS. Let the BS be the origin of our reference frame ($x = y = 0$), and let the arms of lengths l_x and l_y lie across the x and y axes, respectively. Thus, we can write the conditions for completely constructive interference as a func-

9
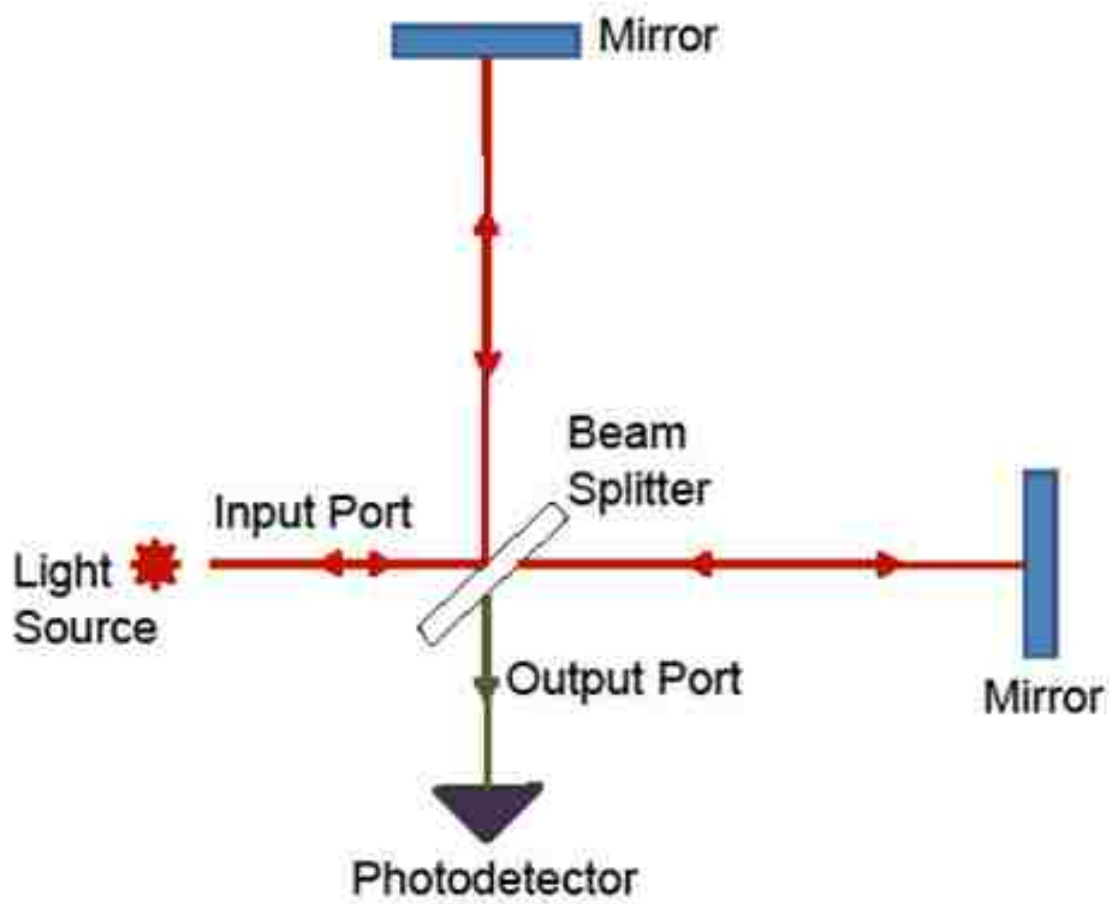
Figure 3.1: Optical layout of a simple Michelson interferometer.

tion of the differential path length ($\Delta l = l_x - l_y$) and the laser wavelength, λ, as $\Delta l = m\lambda$, and the condition for completely destructive interference as $\Delta l = (m + \frac{1}{2})\lambda$ such that $m \in N$. Thus, $(9) - (8)$ shows that the range in differential path length corresponding to phase shift between destructive and constructive interference is one half of the laser wavelength: $\Delta l_{fringe} = \frac{\lambda}{2}$.

Thus, measuring a fine gradient of light intensities between fringes allows the operator of a Michelson interferometer to measure distance fluctuations more precise than the wavelength of the input laser, which at LIGO is $\lambda = 1064$nm. However, even though the LIGO interferometers are large-scale Michelsons are their core, a pure Michelson with $4\,$km arm lengths would not make be capable of making length measurements precise enough to detect gravitational waves. So to increase sensitivity, each arm is made from Fabry-Perot Interferometers.

While at their core, the LIGO interferometers are very large-scale Michelson interferometers, they are much more complex, compound interferometers. Fig. 3.2 shows the optical layout of the Advanced LIGO interferometers, complete with a simple Michelson as well a set of other optical cavities which are vital to detecting gravitational waves.

3.2. Calibration

The LIGO interferometers each have two orthogonal evacuated tubes which each house a Fabry-Perot cavity (arm cavity) approximately 4km in length, and they are extremely sensitive to arm length fluctuations The lengths of the x and y arm cavities are labeled L_x and L_y respectively, and the differential arm (DARM) length is calculated as $\Delta L_{ext} = L_x - L_y$. is calculated as the differential arm length divided by the average arm length. $h = \Delta L_{ext}/\bar{L}$. However, LIGO uses a feedback control loop system to hold the interferometer in its observational state (locked state) by actuating on the test mass positions to cancel out DARM motion, so the calculation of ΔL_{ext} requires one to take into account the effect of the control loop [8] as well as the optomechanical response. This calculation is usually done in the frequency domain by modeling the main components of the control loop as transfer functions, which will be discussed in the following section.

The optomechanical response of each LIGO interferometer is modeled as a transfer function, C; and is referred to as the *sensing function.* The sensing function is used to convert arm displacement
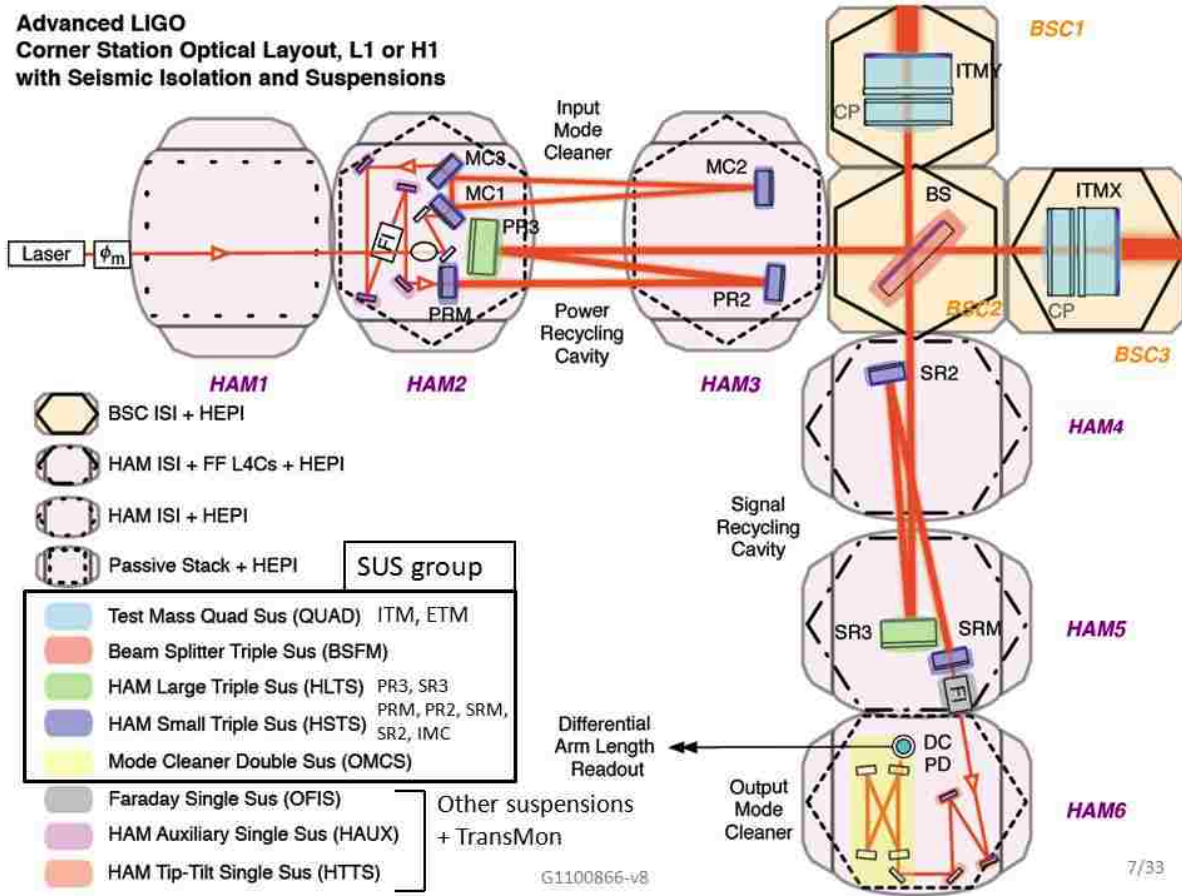
Figure 3.2: Advanced LIGO Optical Layout.
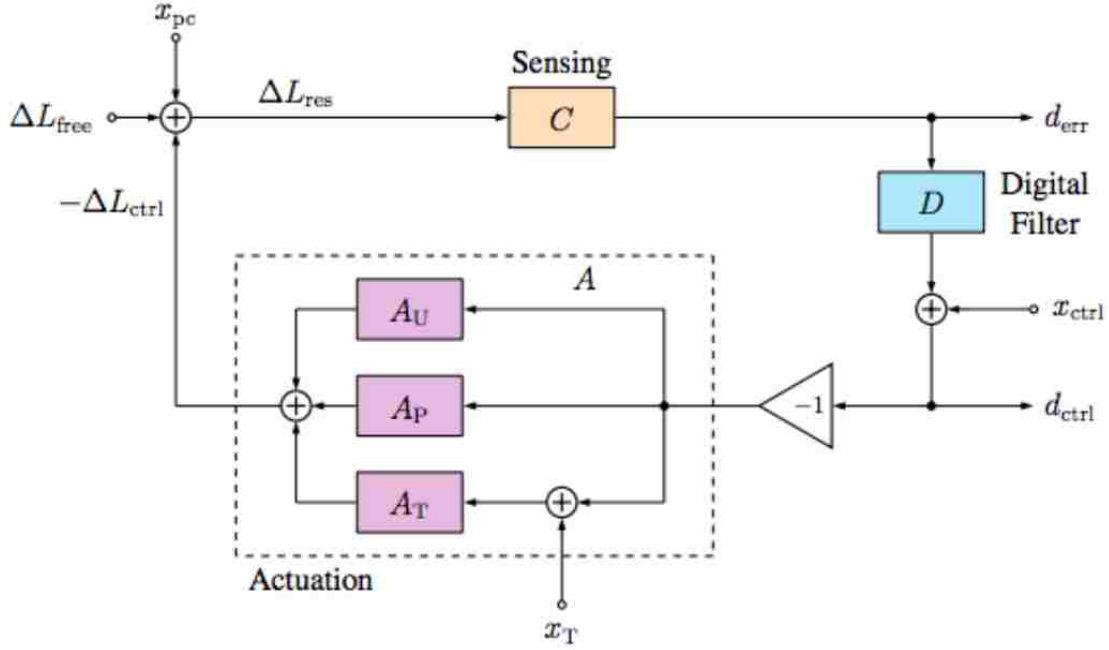
Figure 3.3: Schematic of the Advanced LIGO control loop [9].

differentials into the gravitational-wave (GW) readout signal, DARM ERR (or d_{err}). This signal is fed into digital filter bank (the effect of which are modeled by the transfer function D) to create the DARM-control signal d_{ctrl}. A_U, A_P, and A_T are the *actuation functions*, which model how much DARM displacement (in meters) is induced into the interferometer by feeding d_{ctrl} into the actuators on the bottom three stages of the y-end quadruple suspension, i.e. the *upper-intermediate*, *penultimate*, and *test-mass* stages (Fig. 3.4). Furthermore, the cumulative actuation transfer function *(A)* from all three stages of actuation is written as $A = A_U + A_P + A_T$ [9].

The effect of the control loop on the differential arm length of the interferometer can be expressed as

$$\Delta L_{res} = \Delta L_{ext} - \Delta L_{ctrl} \tag{3.1}$$

where ΔL_{ext} is the DARM displacement caused by an external source –either a GW or noise source–, ΔL_{ctrl} is the DARM displacement induced by the actuators on the bottom three stages of

13
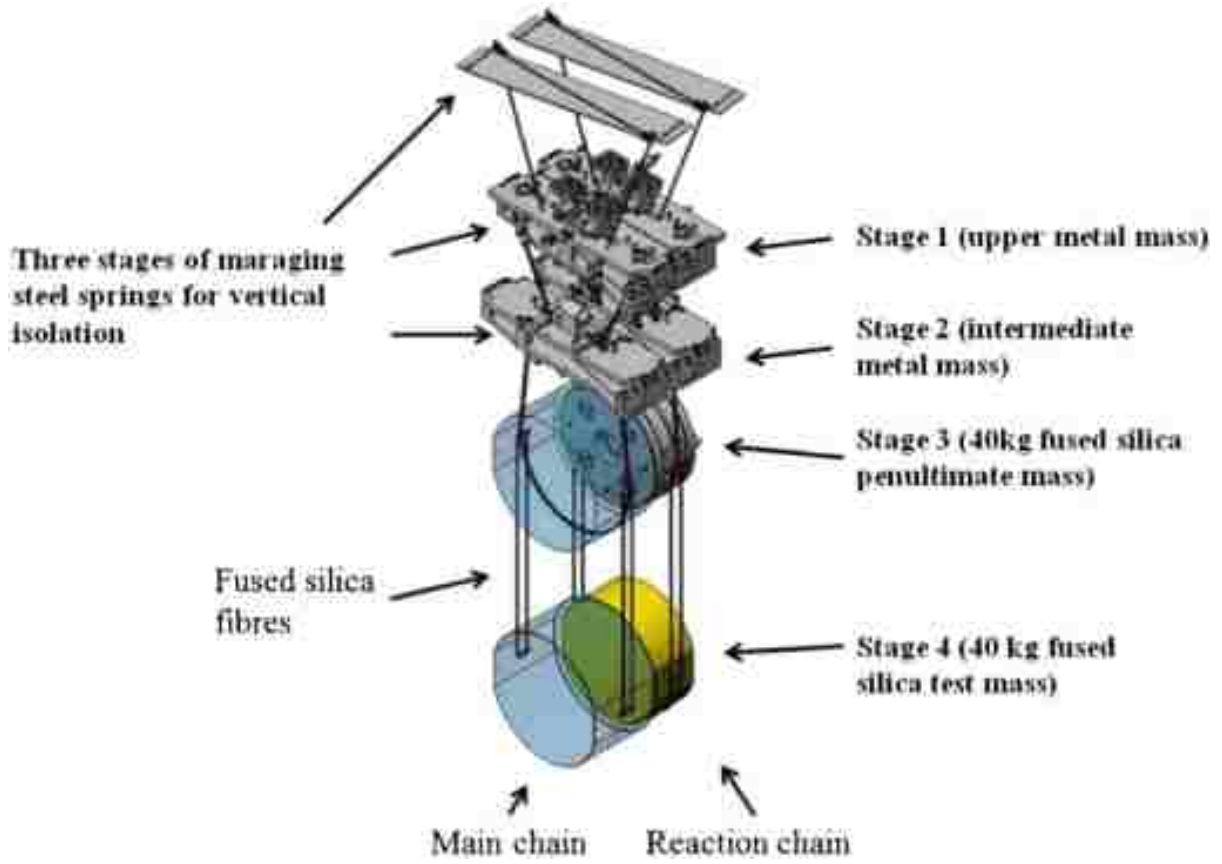
Figure 3.4: Diagram of quadruple suspension isolation system. The four core optics of the LIGO arm cavities are suspended from a four-stage-pendulum isolation system. Actuators on the bottom three stages of the y-end suspension are used to cancel out differential arm length fluctuations [10].

the y-end actuators, and ΔL_{res} is the residual DARM displacement left over after compensation. In order to reconstruct a GW signal, we are interested in calculating ΔL_{ext}.

One can produce an expression of ΔL_{ext} in terms of the d_{err} signal and the transfer functions discussed above:

$$\Delta L_{ext} = \frac{1+G}{C}d_{err} \tag{3.2}$$

where $G = ADC$. Furthermore, the transfer function $\frac{1+G}{C}$ is called the *response function*, and it is used to reconstruct strain from d_{err}.

The LIGO interferometers have a *signal-recycling cavity* placed in the anti-symmetric port of the interferometer which allows for control over the optomechanical response using a scheme known as *Resonant Sideband Extraction* (RSE) [11], and during O2, the signal-recycling cavity was in a zero-detuned configuration, which allows the sensing function to be expressed as a single-pole low-pass filter.

$$C(f) = \frac{K_c}{1+if/f_{cc}}e^{2\pi ifL/c} \tag{3.3}$$

where K_c and f_{cc} are the optical gain and the coupled-cavity pole frequency of the interferometer respectively, and the factor $e^{2\pi ifL/c}$ accounts for the time delay of light traveling down the arm cavities.

The transfer functions discussed in the previous sections are measured by injecting swept-sine signals at certain points in the control loop and measuring the response. This is not possible during observation runs, so "calibration lines" (sinusoidal waves of a constant frequency) are injected into the control loop at various points in the control loop at designated frequencies using different actuators in order to serve as fiducial marks that allow tracking the of the closed-loop transfer function at those frequencies [8, 9].

The PCAL laser is used to actuate on directly on the test mass via radiation pressure, and the signal associated with these lines is labeled x_{pc} [12]. Furthermore, a line is injected into the
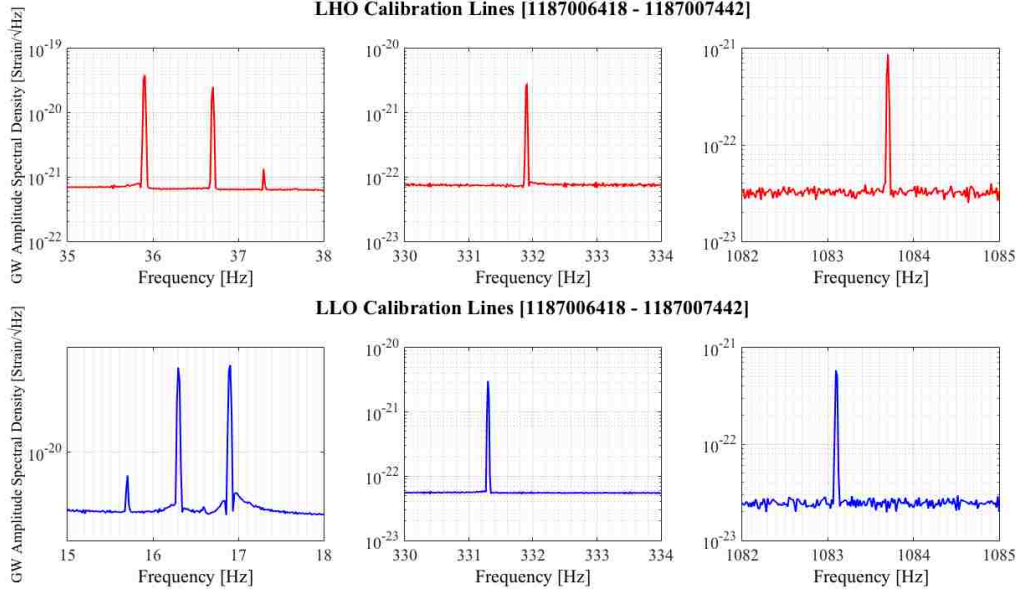
Figure 3.5: Amplitude spectral density plots of calibration lines in GW strain measured at both LHO and LLO detectors calculated using 1024 seconds of h(t) data from August 17, 2017 12:00:00 UTC. The top row (red) show the 5 LHO calibration lines: $x_T(f_T)$, $x_{pc}(f_{pc1})$, and $x_{ctrl}(f_{ctrl})$, such that $f_T = 35.9\,\mathrm{Hz}$, $f_{pc1} = 36.7\,\mathrm{Hz}$, $f_{ctrl} = 37.3\,\mathrm{Hz}$, $f_{pc2} = 331.9\,\mathrm{Hz}$, and $f_{pc3} = 1084\,\mathrm{Hz}$. The bottom row (blue) show the 5 LLO calibration lines: $x_T(f_T)$, $x_{pc}(f_{pc1})$, and $x_{ctrl}(f_{ctrl})$, such that $f_T = 16.9\,\mathrm{Hz}$, $f_{pc1} = 16.3\,\mathrm{Hz}$, $f_{ctrl} = 15.7\,\mathrm{Hz}$, $f_{pc2} = 331.3\,\mathrm{Hz}$, and $f_{pc3} = 1083\,\mathrm{Hz}$.

feedback system on top of the d_{ctrl} signal before it is inverted and fed into the suspension stage actuators; this signal is labeled x_{ctrl}, and a line is injected directly into the electrostatic actuator controlling the y-end test mass; this signal is labeled x_T [9].

The calibration lines are also used for tracking time-dependent variations in the calibration model by comparing amplitude fluctuations in the actuation signals with amplitude fluctuations in sensed by the interferometer in the DARM ERR signal.

The time-dependent calibration model introduces time-dependent parameters into the control-loop transfer functions. For the sensing function C the scaling factor, κ_C, and the coupled-cavity pole frequency, f_{cc}, are allowed to vary in time.

$$C(f,t) = \kappa_C(t)\frac{C_{Res}(f)}{1 + if/f(t)_{cc}} \tag{3.4}$$

where C_{Res} is the residual frequency-dependent sensing function at the reference time.

$$C_{Res}(f) = C_0(f)\Big(\frac{1}{1 + if/f_{cc}(t_o)}\Big)^{-1} \tag{3.5}$$

In addition, the actuation transfer functions for the test mass actuator, κ_{TST}, and the penultimate and upper-intermediate stages, κ_{PU}.

$$A(f,t) = \kappa_{PU}(t)A_{PU}(f,t_0) + \kappa_{TST}(t)A_{TST}(f,t_0) \tag{3.6}$$

The amplitude fluctuations in the calibration injections signals are measured by demodulating the calibration lines. Ratios of the demodulated calibration lines in DARM ERR to their corresponding actuation signals are used to calculate slow-varying measurements of the time-dependent calibration parameters.

Integral to our ability to make astrophysical statements using gravitational-wave detectors are the accuracy and precision with which one can convert the electronic signals outputted by the detectors into gravitational-wave strain, i.e. the calibration of the detectors. The calibration must

take into account the various components of the interferometer as well as the control loop system used to suppress differential arm-length fluctuations.

Over time, the calibration may fluctuate slightly due to various reasons, and so calibration fiducials are used to track these the time-dependence of the calibration during observations on a low-frequency scale [9]. In later chapters, this dissertation will discuss an investigation into this time-dependent tracking method to search for the effect of unveteoed noise transients on the calculation of these parameters and furthermore their effect on gravitational-wave strain reconstruction.

CHAPTER 4. PHOTON CALIBRATOR IMAGE ANALYSIS

4.1. Photon Calibration Overview

The Photon Calibrator uses a laser to exert a force on the end test masses to precisely modulate controlled displacements into the arm-cavity lengths, L_x and L_y, at selected frequencies and amplitudes, which are used as fiducials for calibrating the LIGO control loop [12].

The success of the Photon Calibrator as a reliable fiducial is dependent on the confidence of our knowledge of the power the PCAL beams incident on the test mass, and furthermore our ability to model the transfer function which maps beam power to displacement induced in the arm cavity.

The PCAL laser actuates on the test mass via radiation force which we express in terms of the incident power, $P(t)$ and optical efficiency of the mirror, $0 \leq \epsilon \leq 1$.

$$F_{rad}(t) = \frac{(1+\epsilon)P(t)}{c} \tag{4.1}$$

The PCAL laser is capable of outputting 0W to roughly 2W of power and during operation, the power is modulated around 1W. Thus we can write the power incident on the test mass as

$$P(t) = P_m(1 + \beta \cos(\omega t)) \tag{4.2}$$

where $P_m \approx 1W$, and $0 \leq \beta \leq 1$ is the modulation depth. It is interesting to derive the response of the test mass to an actuation force.

The test mass hangs at the bottom of a quadruple pendulum. The response of a quadruple pendulum to a driving force is quite complicated in general, and the LIGO Calibration team takes the full quadruple-pendulum response into account. However, for modulation frequencies greater than $\approx 10Hz$, the response of a pendulum behaves like a free mass. The lowest PCAL injection frequency is $\approx 30Hz$, so this allows us to approximate the system to that of a free body being acted upon by an external force. Consider a free particle of mass, m, initially at rest at the origin

that undergoes a sinusoidal external force $F = F_{rad}(t)_{\omega>w_0}$, one can ignore the DC component of F_{rad} and express the acceleration of the particle as

$$\ddot{x}(t) = \frac{(1+\epsilon)P_m\beta}{mc}\cos(\omega t) \tag{4.3}$$

And from this one can integrate to obtain the equation of motion:

$$x(t) = -\frac{(1+\epsilon)P_0}{mc\omega^2}\cos(\omega t)\cos(\theta). \tag{4.4}$$

Here, P_m and β are combined into P_0, and with a convenient choice of initial conditions, the constants of integration are made to vanish. Additionally, $\cos(\theta)$ is applied to account for the fact that the PCAL beams come in from the side at an angle of $\theta \approx 9.8°$. Using this expression we can calculate amplitude length modulation induced into the arm cavity given the power and frequency of the input PCAL laser.

This approximation is tailored for a point-particle test mass. If we require a more accurate representation of the physics in play, we can account for the soft-body deformation of the test mass surface [13] as well as the rigid body mechanics of the test mass as both phenomena contribute to the calibration uncertainty when the PCAL beams are misaligned. The latter case is discussed in the following section.

4.2. Uncertainty Induced by Beam Spot Misalignment

If the PCAL actuation point is directly through the center of mass of the mirror, then we should expect the modulated arm length to exactly match the above expression. However, a misaligned actuation point can introduce rotation, adding systematic error to the calibration.

The face of the test mass can be considered as a plane characterized by a Cartesian reference frame with its origin positioned at the center of mass of this plane. We assume the PCAL beam paths are parallel to the optical axis of the test mass. We let the points at which the PCAL beams contact the surface of the test mass be $\vec{a}_1$ and $\vec{a}_2$ and the power amplitudes of each beam be P_1

and P_2, and define an effective actuation point, $\vec{a}_{eff}$, which is the power-weighted average of $\vec{a}_1$ and $\vec{a}_2$,

$$\vec{a}_{eff} = \frac{P_1\vec{a_1} + P_2\vec{a_2}}{P_1 + P_2} \tag{4.5}$$

If the PCAL actuation point is off-center, but the LIGO interferometer beam is perfectly centered, then we should not expect additional displacement "seen" by the detector. If however the actuation point and the interferometer beam are both off-center, then induced rotations will couple into the interferometer signal, confusing the calibration. The amplitude of induced rotation is the ratio of the mirror mass to its moment of inertia times the dot product of the positions of the effective actuation point and the position of the center of the interferometer beam.

$$x_{rot} = \frac{M}{I}\vec{a}_{eff} \cdot \vec{b} \tag{4.6}$$

Given the beam positions ($\vec{a_1}$, $\vec{a_2}$, and $\vec{b}$) one may estimate the amplitude of displacement induced by a small misalignment of the PCAL beams with the following equation:

$$x_0 = -\frac{(1+\epsilon)P_0\cos(\theta)}{mc\omega^2}(1 + \frac{M}{I}\vec{a}_{eff} \cdot \vec{b}). \tag{4.7}$$

The end-station of each arm cavity was equipped with an in-air camera that would peer into the vacuum chamber via a periscope and look at the surface of the test mass. Using these cameras I was able to take photographs of the test mass surfaces in order to estimate the beam locations. The photographs were 6000x4000 pixel arrays, so my methodology involved constructing a transformation of the image basis in pixels to a positions on the surface of the test mass (Fig. 4.1 and Fig. 4.2). The test mass surface should appear circular when viewed head-on and elliptical when viewed at an angle. Given that the test masses have precisely-known diameters ($\approx 340\,\mathrm{mm}$), and that they are being viewed by the camera at an incident angle of 8.75°, I was able to measure the positions of the PCAL beams by fitting a set of points in the images corresponding to the visible edge of the test mass to a ellipse, and using the fitted ellipse parameters to construct a
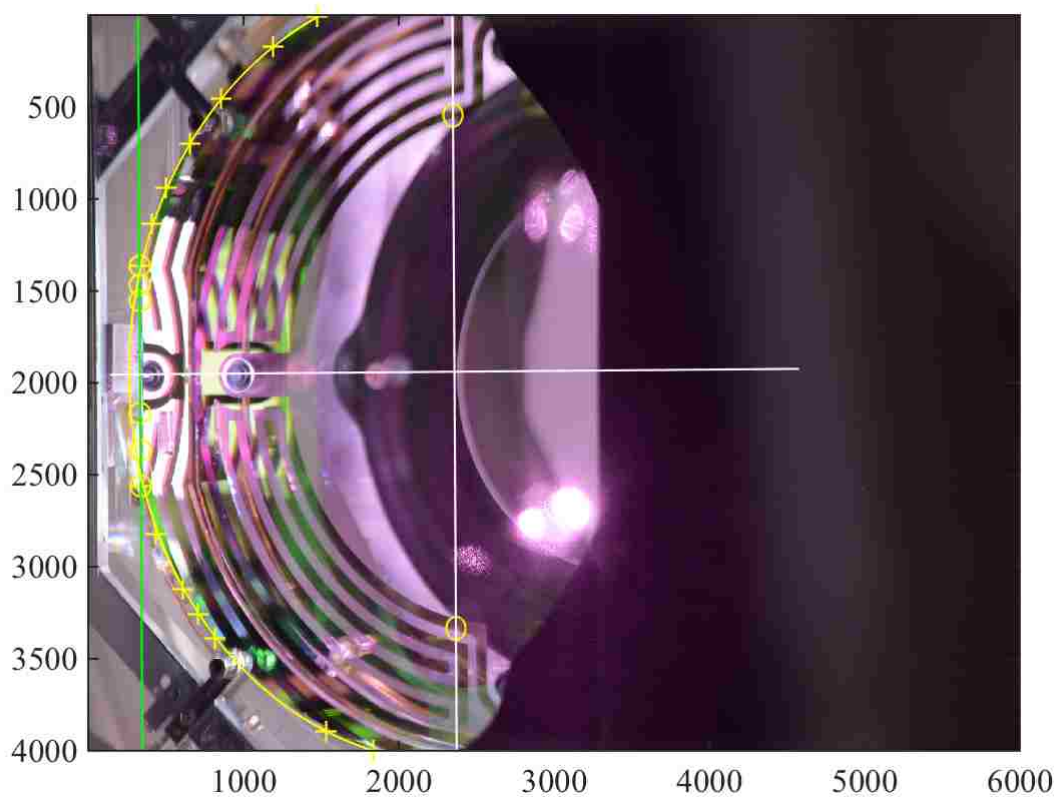
Figure 4.1: Fit of LHO x-end test mass illuminated to see the edge clearly. Yellow crosses and yellow circles are the points chosen for the curved edge and the flat edge, respectively. The smooth curve is the elliptical fit, and the coordinate system set to the center of ellipse found by fitting.
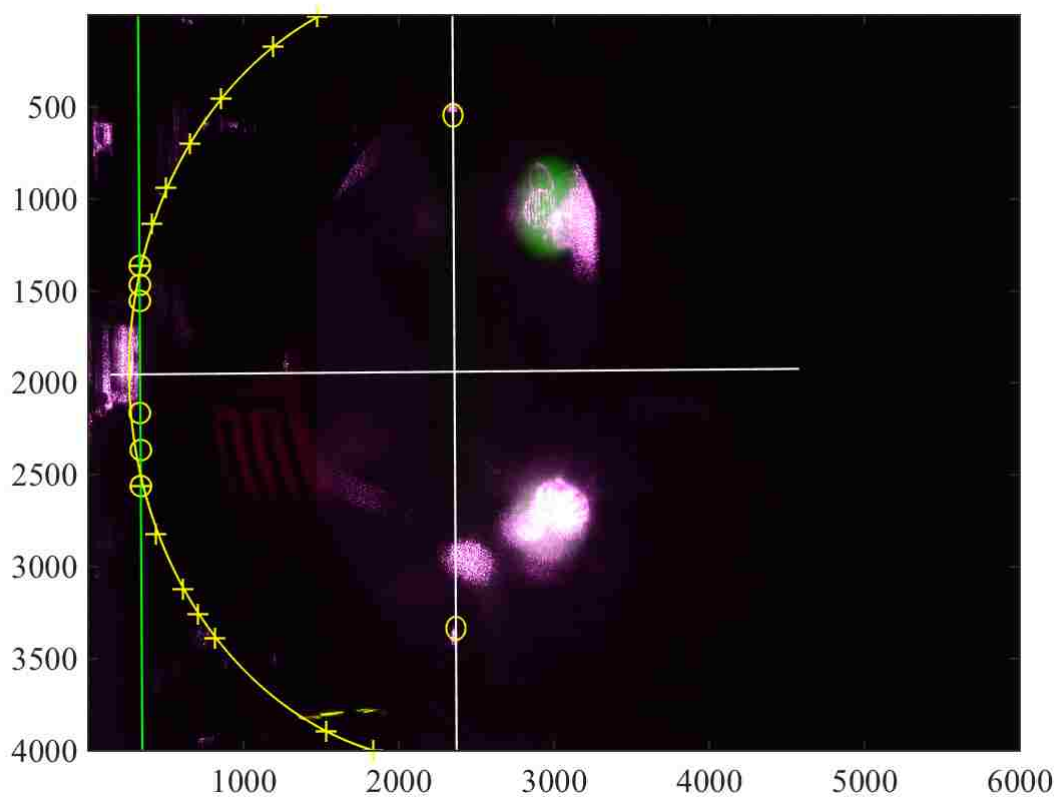
Figure 4.2: Fit of LHO Y-end test mass in dark chamber, so PCAL beam spots (circled) are visible.

transformation from the photograph basis to the test-mass basis. Tab. 4.1 shows an example of the measurements of these beam positions in mm [12].

Figure 4.3: Example of long-exposure photograph of the interferometric-beam scatter from the surface of a test mass.

Furthermore, the position of the interferometric beam $\vec{b}$ is also needed to estimate the rotational uncertainty. Thus, I also took long-exposure photographs of the test-mass surfaces while the arm cavities were in lock (Fig. 4.3). I estimated the position of the interferometric beam in the image basis by first cropping out unrelated features from the photograph and omitting saturated pixels. Then I fit the 2-dimensional image arrays to a 2-dimensional Gaussian distribution to obtain fitted parameters associated with the center of the beam-scatter distribution in pixels. Then I used the basis transformation constructed with the previous photograph to ascertain the center of the inteferometric beam in the test-mass basis. Finally, with all the beam positions estimated, I made estimates of uncertainty due to rotation induced from beam misalignment.
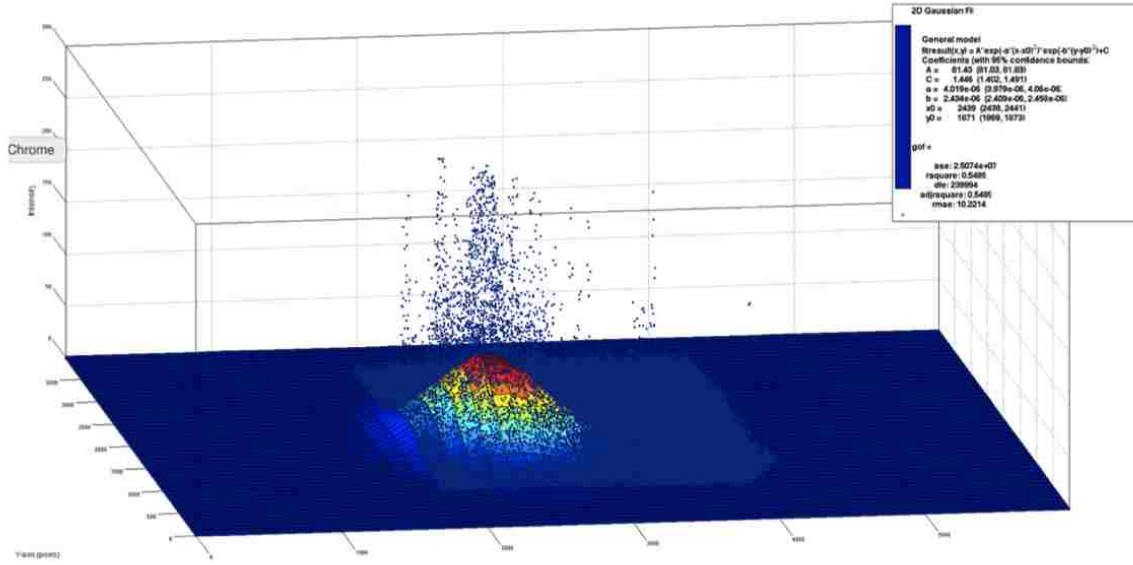
Figure 4.4: Example of 2D image array fit to 2D Gaussian distribution to estimate the interferometric beam center $\vec{b}$.

Table 4.1: Example of image-analysis measurements of PCAL beam offsets in mm.

Offset (mm)	LHOX	LHOY	LLOX	LLOY
$\vec{a}_1$	(-1.7, 4.4), (-4.6, 7.3)	(-0.2, 2.9)	(0.0, -2.4), (-1.2, -2.8)	(3.9, 0.0)
$\vec{a}_2$	(-4.2,-1.8), (-4.3, -3.9)	(-1.1, -3.6)	(-2.4, 1.7), (-5.1, 1.7)	(1.4, 5.5)

I carried out this process each time the PCAL beams were adjusted and intermittently to account for any changes that would possibly occur over the course of several weeks, and in the most significantly misaligned cases I observed, the PCAL beams were misaligned by approximately 3 mm and the interferometric beam by approximately 10 mm. This should induce rotations that would contribute an error of 0.1% in the PCAL, which is small compared to the error expected from bulk elastic deformation [13].

CHAPTER 5. TIME-DEPENDENT PARAMETER TRANSIENTS FOR O2

The time-dependent calibration parameters are known to vary slightly during observation runs, and they are tracked and compensated for faithfully on slow time scales. However, this search method was designed for the purpose of finding transients on minute time scales. We have developed and implemented a new method for identifying statistically significant transients in the time-dependent calibration parameters, which was applied to O2 data to search for transient events and to ascertain the overall effect on the calibration uncertainty for the Hanford and Livingston detectors.

5.1. Modified Z-score
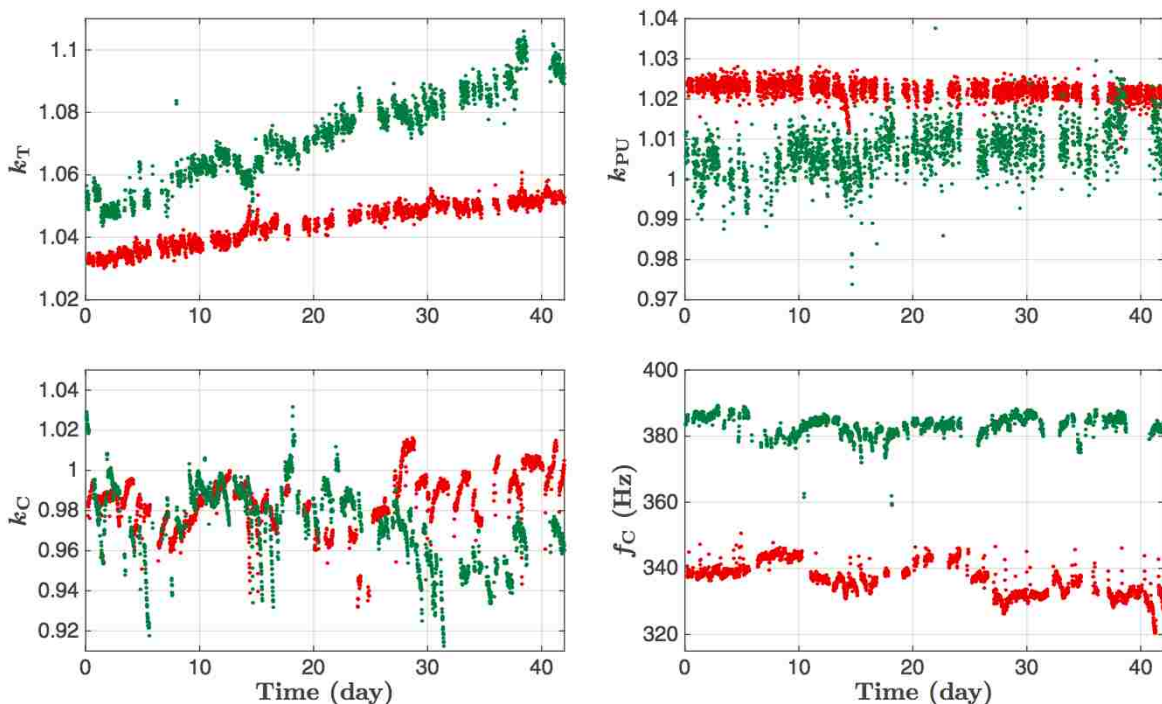
Figure 5.1: DARM time-dependent parameters calculated from calibration lines–LIGO Hanford (red traces) and LIGO Livingston (green traces). Nominal values of all three scalar factors κ_{TST}, κ_{PU} and κ_C are 1, and the nominal value of the coupled cavity pole frequency, f_{cc}, for LIGO Hanford is 341 Hz and for LIGO Livingston is 388 Hz [9].
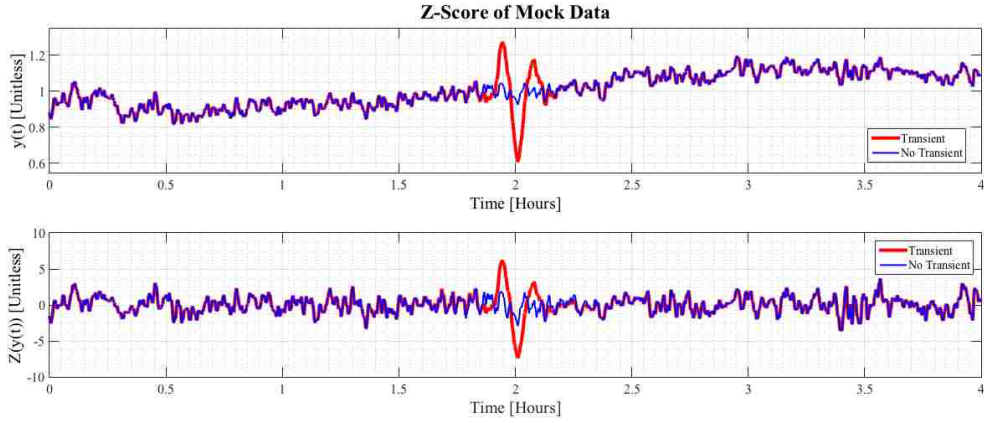
Figure 5.2: Example of the z-score algorithm applied to mock non-stationary data. Comparison of mock data with and without a large transient at t = 2 hours.
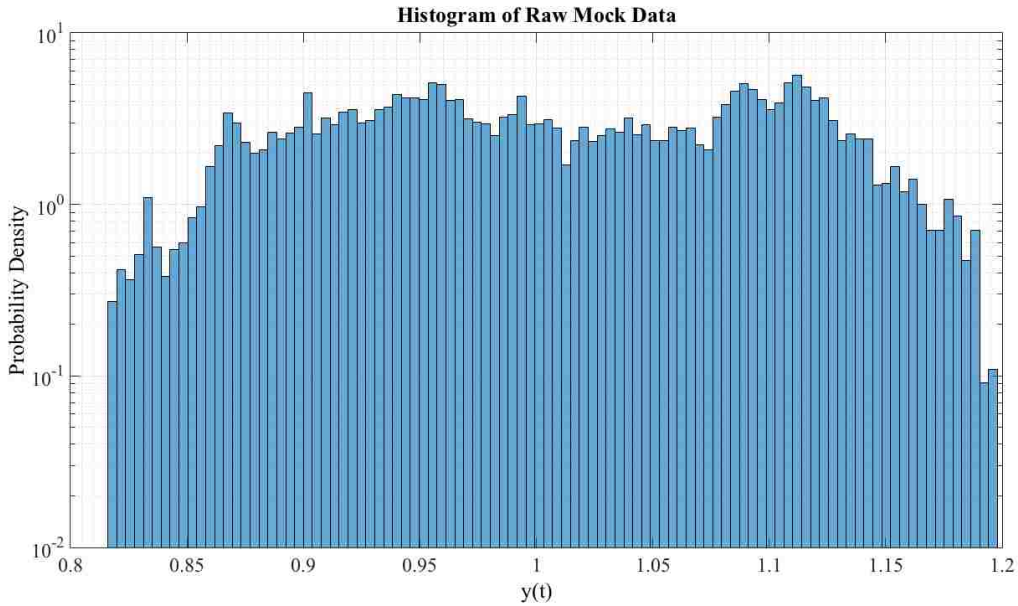
Figure 5.3: Probability density histogram of raw mock data. The distribution is spread over a wide set of values. This makes setting thresholds for defining large fluctuations difficult.

Fig. 5.1 shows the values of the time-dependent parameters over a 45-day period during O2. It is evident from this figure that the behavior of the time-dependent parameters is non-stationary on a days-to-weeks timescale. These are the slowly-varying changes being tracked by the time-dependent parameters. We want to find out if there are short-duration transients that are not being tracked faithfully. Thus, we applied a transformation on the time-dependent parameter data that will remove the non-stationarity of the data over long timescales and establish a standardized metric of the statistical significance of each datum.

In particular, the sweeping time-window used in this analysis was a ±15-minute window surrounding each datum that was used to calculate the modified z-score of the datum. That is, for each 30-minute set of data, X, surrounding datum, x_c and consisting samples $x_1, x_2, ..., x_c, ..., x_N$, then the z-score corresponding to the data point in the center of the data segment, x_c can be written as

$$z_c = \frac{x_c - median(X)}{\alpha * median(abs(X - median(X)))} \tag{5.1}$$

where $\alpha = 1.253$ to scale the resulting distribution to have a standard deviation of 1. A 30-minute window was chosen to be long in compared to the upper-limit frequency of the time-dependent parameters (7.8 mHz), but short compared to the average lock segment duration (approximately 3 hours). In order to illustrate the behavior of this algorithm, Fig. 5.2 shows a time series plot of artificially-created non-stationary data compared to a time series plot of the z-score of that data. In both plots, overlapping traces compare the raw data to the raw data with the addition of a large transient at t = 2 hours. the effect of the z-score is to remove the slowly-varying factors while preserving the transient. Fig. 5.3 shows the histogram of the raw mock data with a transient. Since the data are non-stationary, the distribution is spread out, obscuring the transient and making it difficult to apply meaningful statistical thresholds. On the other hand, Fig. 5.4 shows the histograms of the z-scores of the mock data without a transient and with a transient. In the former case, the distribution of the z-score is mostly consistent with a Normal-Gaussian

distribution. This is also true in the latter distribution; however, the effect of the transient stands out above the background.

Even though replacing all the median operations in our definition of z with means would be more computationally efficient, the use of medians in the algorithm makes the standard deviation of resultant z-score data resilient against the effect of large but short transients. Fig. 5.5 shows time series of the z-score of our mock data using medians compared with a mean-based method. Since z is inversely proportional to the mean absolute deviation from the mean, the presence of a large transient in the input window diminishes the result, producing z-scores where the transient is attenuated.
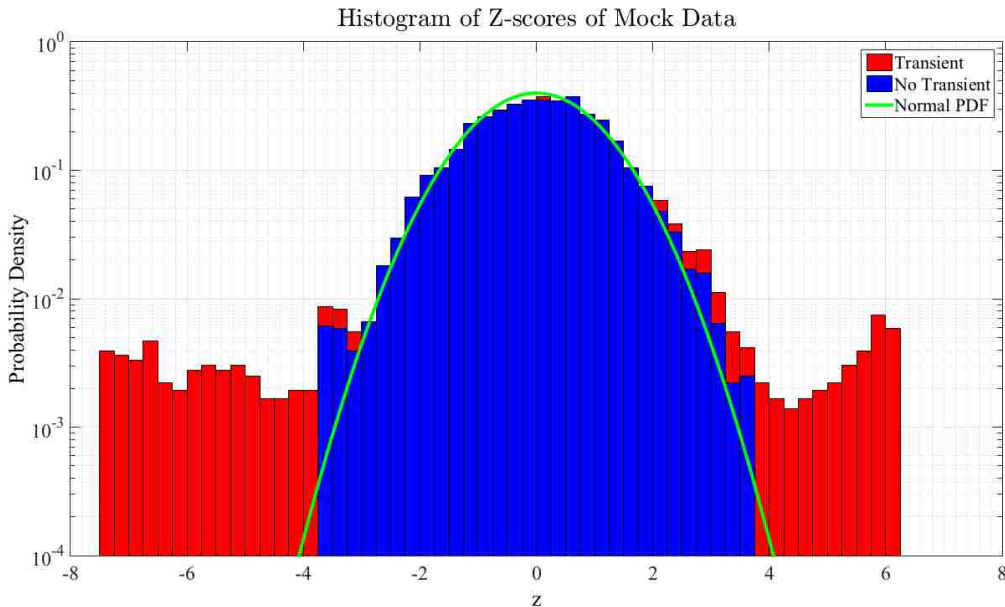
Figure 5.4: Probability density histograms comparing the distributions of z-score data from mock data without the transients to the distribution of z-scores of mock data with the transient.

Z-score data spanning O2 were calculated for each time-dependent calibration parameter and were used to classify the statistical significance of the corresponding data point of the time-dependent calibration parameter within the temporal vicinity of the data point in question.

Since time-dependent parameter values are expected to fluctuate within a few minutes of the interferometer acquiring or losing observational state (losing lock), z-scores within 15 minutes of a

Figure 5.5: Time series comparing z-scores of mock data using a mean-based method with z-scores using a mean-based method.

lock acquisition or loss are omitted. Likewise, data within 15 minutes of known data quality vetoes are omitted in order to focus our analysis on new transients.

Finally, thresholds of ± 5 were applied to the z-scores to group data segments into distinct transient events. When the absolute value of a z-score exceeds the threshold, this marks the beginning of a new transient event, and when it eventually falls below the thresho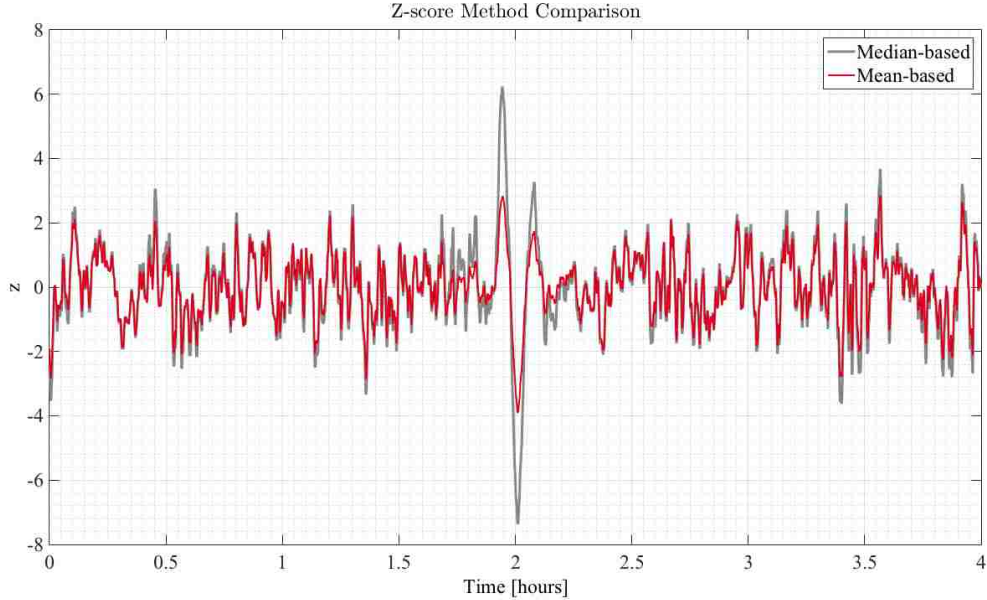ld, this marks the end of the event. This is applied to z-score values of each time-dependent parameter to produce a list of new parameters (i.e. the start time, the end time, the maximum z-score, and the time corresponding to the maximum z-score), which describe a transient event.

5.2. Characterizing Transients

Advanced LIGO's 2nd Observation Run (02) occurred from November 30, 2016 16:00:00 UTC to August 25, 2017 22:00:00 UTC, spanning 168 days and 6 hours; however, LHO was in an operational state 61.7%, while LLO was in an operational state 60.6% of the time. Taking into account the 15-minute padding around observing segments and data-quality veto segments, our analysis calculated z-scores for 66.6% of the total time-depedent calibration parameter data corresponding to LHO observational time and 79.2% of LLO observational time. Due to the nature of the z-score

algorithm, slowly varying drifts were removed, and the resulting distributions were mostly consistent with a Normal Gaussian distribution. However, the distributions of some parameters show evidence of noise transients that vary quickly compared to the timescale of a typical observation stretch, which on average lasted approximately 3 hours.

As described in section 5.1, the z-scores for each parameter were then scanned for instances when $|z|$ passed our threshold of 5 and returned back under it. Each such instance we regard as a potential noise transient. Table 5.1 enumerates the number of noise transients that were detected by our algorithm for each parameter, which will be discussed in the following subsections.

Table 5.1: Break down of the number individual noise transients isolated by our algorithm using an $|z| \geq 5$ threshold. The first column lists the parameter symbols. The 2nd and 4th columns list the number of transients found by our method during O2 for LHO and LLO respectively. The 3rd and 5th columns list the percentage of the total O2 observational time for LHO and LLO respectively.

Parameter	No. at LHO	% of O2 (LHO)	No. at LLO	% of O2 (LLO)
f_{cc}	51	0.0098	86	0.0299
κ_C	30	0.0065	97	0.0359
κ_{PU}	44	0.0064	56	0.0137
κ_{TST}	45	0.0089	68	0.0138
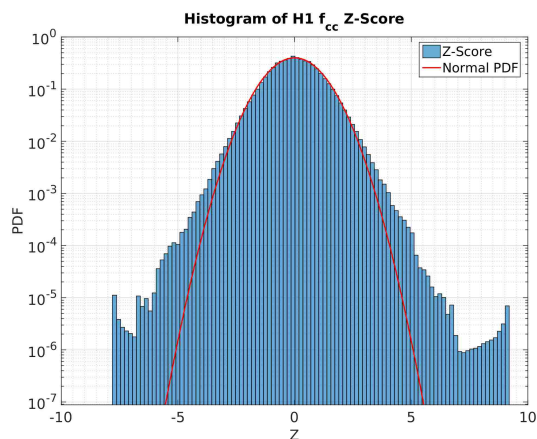
(a) f_{cc} z-score distribution of LHO O2 data
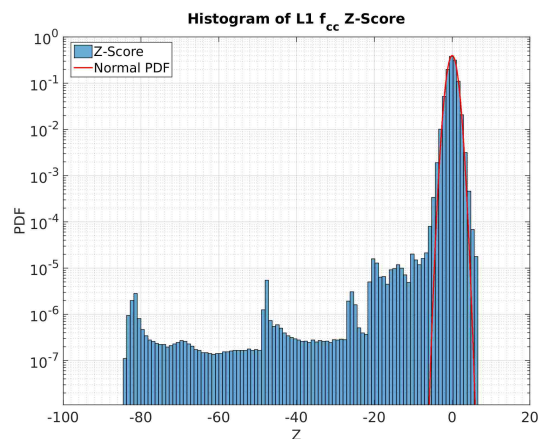
(b) f_{cc} z-score distribution of LLO O2 data.

Figure 5.6: Histograms of f_{cc} z-scores using O2 data from LHO *(left)* and LLO *(right)*. These plots show that the vast majority of data points fit within a Normal Gaussian distribution centered around a null z-score; however, in the LLO data, several large excursions are evident, which are indicative of significant outlier events in the LLO coupled cavity pole frequency estimates.

As expected, the results of the z-score calculations of f_{cc} are consistent with a Normal distribution (Fig. 5.6). The noise transients found for LHO all have peak z-score magnitudes between 5 and 10 (Fig. 5.7), and while the vast majority of the f_{cc} transients found from LLO data have peak z-score magnitudes between 5 and 10, there is a spread of a small number of transients with z-score magnitudes up to nearly 85. The analysis found 86 significant noise transients. The largest had a peak z-score magnitude of $|z| = 83.71$ for 199 seconds from 1168962803 to 1168963002 GPS, and the second largest $|Z| = 48.25$, which lasted 158 seconds from 1168961184 to 1168961342 GPS. Fig. 5.8 shows the time series plot of the two largest noise transients that were identified by our method. An offline, high-frequency recalculation of f_{cc} shows little difference in the shape of the transients, except that the offline calculations peak at a higher value because the online parameters are held constant when the calibration line uncertainties are high, and that the transients peak sooner because the broader demodulation bandwidth used in the calculation of the offline parameters allow for faster responses.
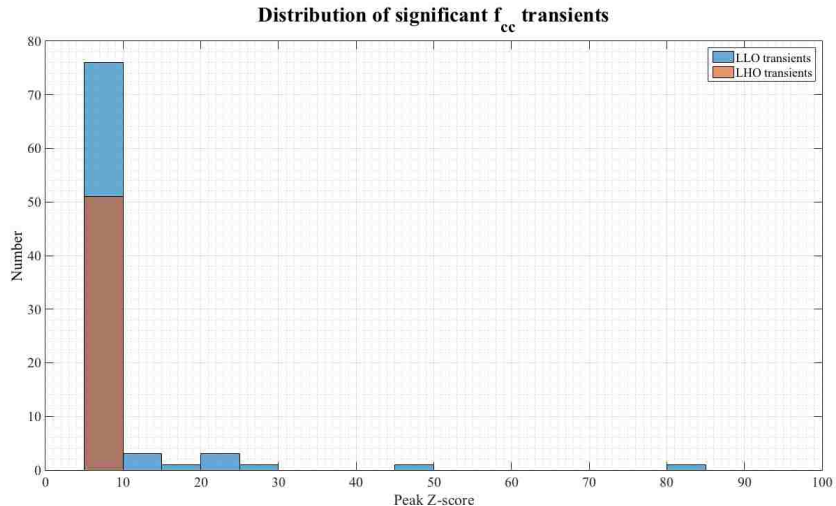
Figure 5.7: Comparison of distributions of peak z-score magnitudes for f_{cc} at LHO and LLO.

The results of the z-score calculations of κ_C are consistent with a Normal Gaussian distribution with signs of a few significant outlier events. Fig. 5.9 shows that the noise transients found for LHO all have peak z-score magnitudes between 5 and 10, while the LLO results reach z-score magnitudes to almost 64. Overall, the analysis found 97 significant noise transients, the largest had a peak z-score magnitude of $|z| = 55.46$ and was above the $|z| \geq 5$ threshold for 190 seconds

Figure 5.8: Timeseries plot of the LLO f_{cc} centered around the peak time corresponding to the largest f_{cc} z-score event throughout O2 (January 20, 2017 15:53 UTC). The orange trace illustrates the data calculated by the calibration pipeline with an upper frequency cutoff at 7.8mHz. The blue trace illustrates the reconstructed data with an upper frequency cutoff at 0.3Hz. The high-frequency reconstructions are not appreciably difference from the original calculations. The high-frequency reconstruction shows the interferometer coupled cavity-pole frequency quickly dropping about 125 Hz over the course of about 3 minutes.
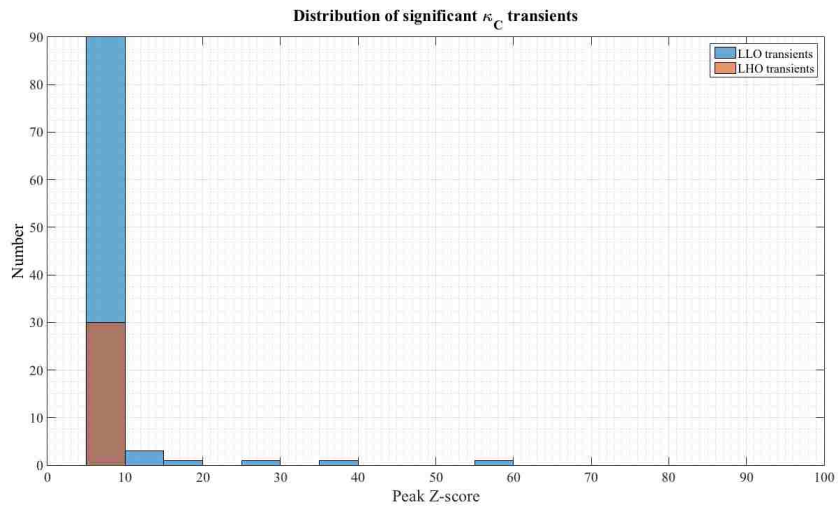
Figure 5.9: Comparison of distributions of peak z-score magnitudes for κ_C at LHO and LLO.
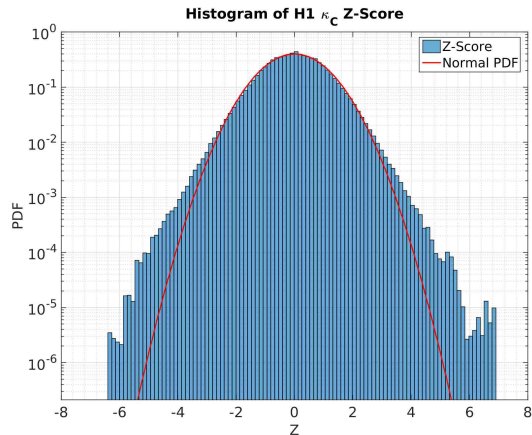
(a) κ_C z-score distribution of LHO O2 data.
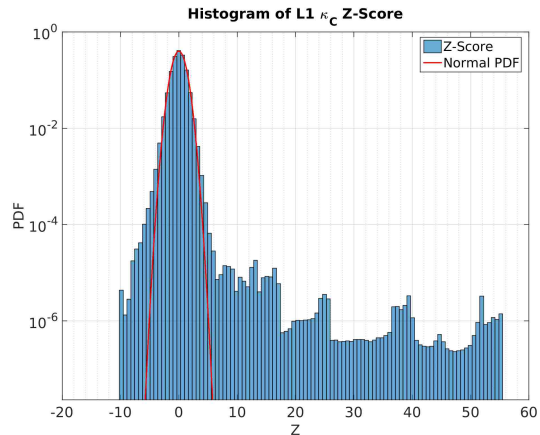
(b) κ_C z-score distribution of LLO O2 data.

Figure 5.10: Histograms of κ_C z-scores using O2 data from LHO *(left)* and LLO *(right)*. Similarly to the f_{cc} z-scores, κ_C z-scores are largely Normal Gaussian with a mean of zero, but a number of large excursions are evident from LLO data.

from 1168962803 to 1168962993 GPS. The second largest transient found had a peak magnitude z of $|Z| = 39.45$, which lasted 148 seconds from 1168961194 to 1168961342 GPS. These transients overlap in time with the top 2 largest noise transients found in the f_{cc} parameter. Fig. 5.11 is a time series plot of these two loudest transients. It makes a comparison of the online κ_C with our offline high-frequency recalculation. Like in the case with the 2 loudest transients in f_{cc}, there is not much difference in the overall shape of the transients, other than the offline recalculations peak higher and sooner.

The coefficient that tracks fluctuations in the actuation transfer functions of both the upper-intermediate and penultimate suspension stages, κ_{PU}, had z-score distributions very consistent with Normal Gaussian data. Fig. 5.12 shows that the z-scores of κ_{PU} at both detectors show little evidence of significant transients that may have had a strong effect on the calibration. For LHO, we only found 44 transients in κ_{PU} with peak z magnitudes $|z| \geq 5$; however, the most significant transient peaked at only $|z| = 6.73$. For LLO we found 56 transients. The largest had a peak z magnitude of only $|z| = 7.13$.

The z-score results for the coefficient that tracks the actuation transfer function were indicative of a well-behaved test-mass actuation function at both detectors. The distributions of its z-score
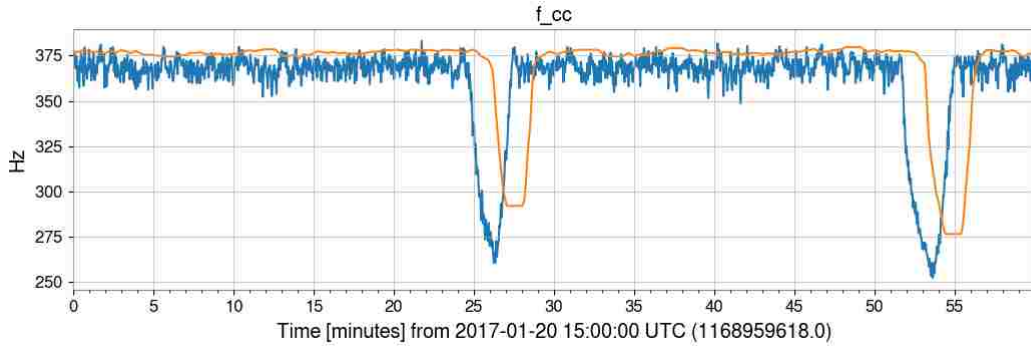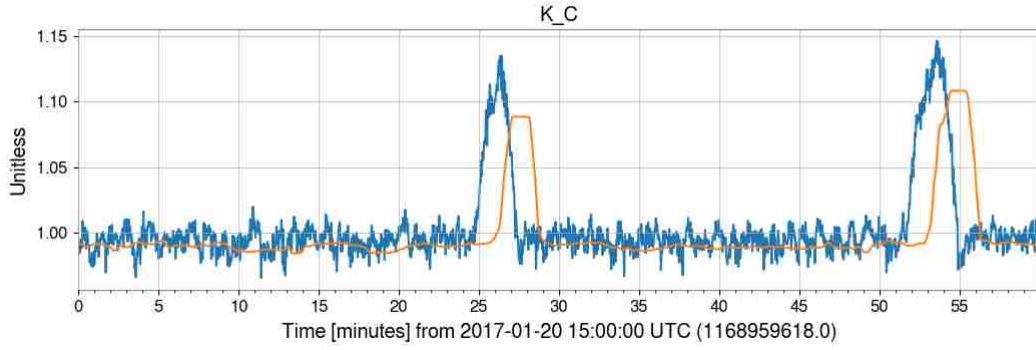
Figure 5.11: Time series of the LLO κ_C centered around the peak time corresponding to the largest f_{cc} z-score event throughout O2 (January 20, 2017 15:53 UTC). The orange trace illustrates the data calculated by the calibration pipeline with an upper frequency cutoff at 7.8mHz. The blue trace illustrates the reconstructed data with an upper frequency cutoff at 0.3Hz. This plot shows the optical gain increased by about 15% over the same period of time that the coupled-cavity pole frequency decreased appreciably.
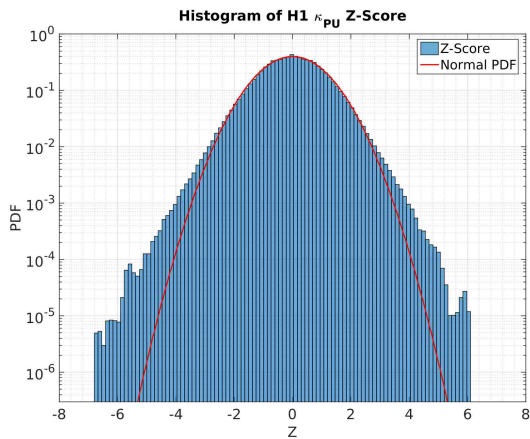
(a) κ_{PU} z-score distribution of LHO O2 data.
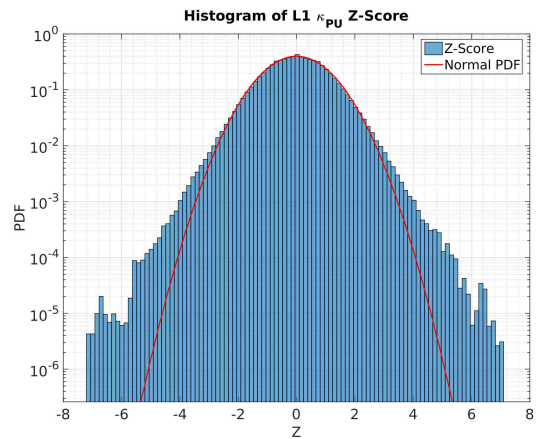
(b) κ_{PU} z-score distribution of LLO O2 data.

Figure 5.12: Histograms of κ_{PU} z-score distribution of O2 data from LHO *(left)* and LLO *(right)*.
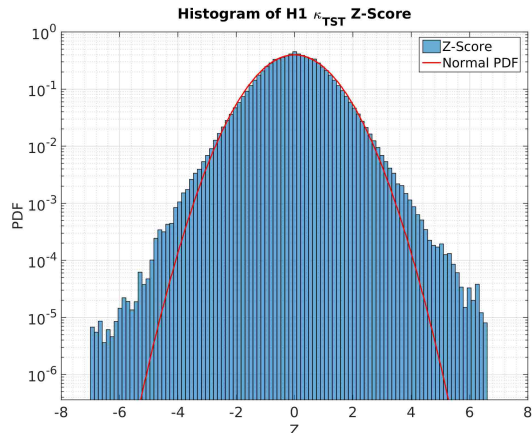
(a) κ_{TST} z-score distribution of LHO O2 data

(b) κ_{TST} z-score distribution of LLO O2 data.

Figure 5.13: Histograms of κ_{TST} z-score distribution of O2 data from LHO *(left)* and LLO *(right).*

are consistent with Normal Gaussian random data with rare exceptions for both LHO and LLO. At the LHO detector, the there were 45 transients found in κ_{TST}, and the peak z-score magnitude was only $|z| = 7$. Likewise, the test-mass actuation function was well behaved at the LLO detector. κ_{TST} was found to have 68 transients; however, the largest only went up to $|z| = 7.04$.
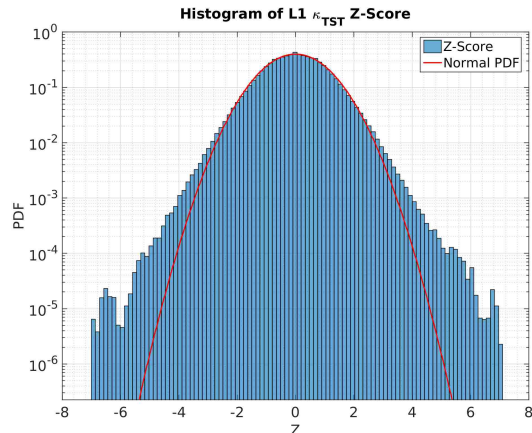
5.3. Effect of Largest O2 Calibration Transients on Calibration Uncertainty

Large fluctuations in one or more time-dependent calibration parameter coincident with a gravitational-wave detection has the potential to affect the uncertainty in modeling the calibration response function, which would contribute to uncertainty in astrophysical parameter estimations. None of the noise transients found by the method described in this paper were coincident with any of the confirmed gravitational-wave signals nor the marginal candidates of O2. We assess what is the effect that the worst offenders had on strain reconstruction to evaluate the impact on parameter estimation of gravitational-wave sources in the future, when frequent detections will make overlap more likely.

On January 20, 2017, the two events with the highest corresponding z-scores occurred in both the f_{cc} and κ_C parameters. (Figs. 5.8 and 5.11) show the time series data of f_{cc} and κ_C, and (Fig. 5.15) shows two periods of about 10 minutes of highly elevated noise in the calibrated gravitational-wave strain below approximately 30Hz, which are coincident with the transients. It

is likely the elevated low-frequency noise contaminated the time-dependent calibration parameter calculation through the 3 lowest calibration lines. Similar coincident noise behavior was observed in the detector output, in core optic motion measured via optical laser, as well as accelerometer data. This indicates that the large fluctuation in the coupled-cavity pole frequency and optical gain coefficient is caused by seismic activity raising the overall noise level in detector output across a frequency band which overlaps calibration lines, contaminating the calculation of the parameters.

In order to quantify the effect these noise transients had on the calibration, we compared the systematic error $\delta R/R^{model}$ and uncertainty σ_R/R^{model} [14] calculated five minutes before and during the central time of each of the noise transients (Fig. 5.14). In all four cases, the regime of the detector's most sensitive band (150 Hz), the 1σ uncertainty thresholds were found to increase modestly during loud the noise transients, increasing the 1σ uncertainty in the calibration from from 1.2% to 3.4%.
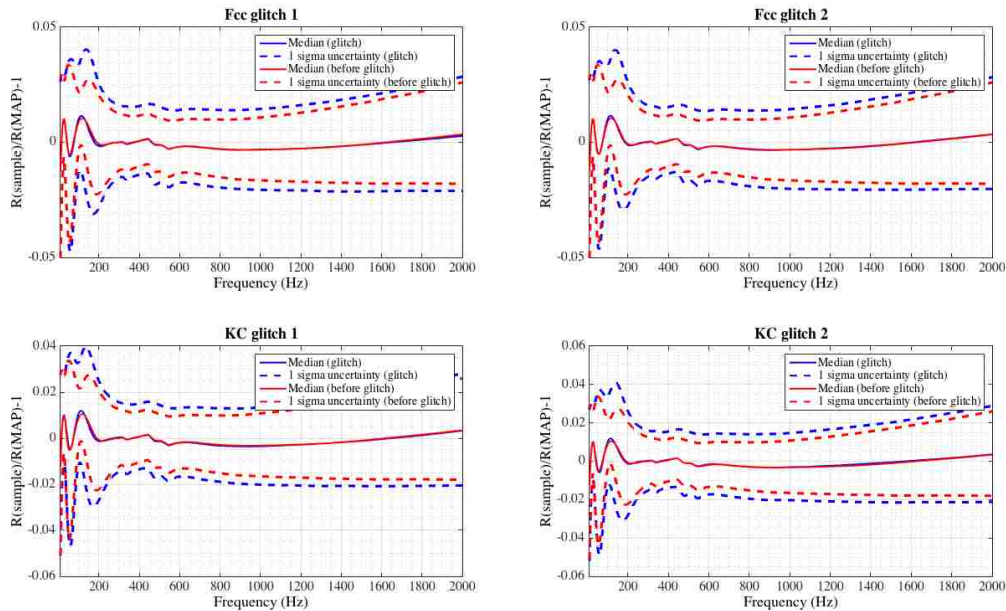
Figure 5.14: Comparison of the calibration response function residuals during the most significant noise transients.
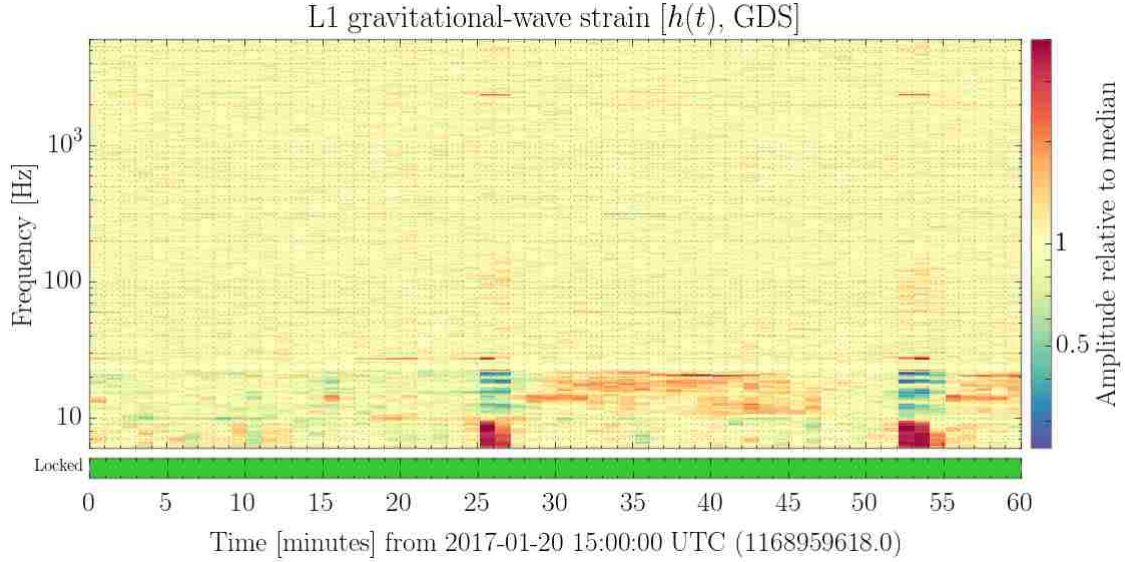
Figure 5.15: Normalized spectrogram of gravitational-wave strain surrounding the January 20, 2017 events. Each amplitude value has been normalized by the median value of its corresponding frequency bin. This figure shows two periods of highly elevated low-frequency noise, which are coincident with the two time-dependent calibration parameter noise transients in question, and overlap with three calibration lines.

5.4. Conclusions

This analysis demonstrates that the time-dependent calibration tracking system operating with good fidelity during O2. No serious transients were found in the LHO calibration parameters, and only 4 potentially serious transients were found in the coupled-cavity pole frequency and optical gain parameters for LLO. Even so, these transients have minimal impact on the calibration uncertainty in the interferometer's detection band.

CHAPTER 6.   ANALYSIS OF O3A

6.1.   Characterizing Transients

The first phase of Advanced LIGO's 3rd Observing Run (O3a) lasted 184 days from April 1, 2019 15:00:00 UTC to October 1, 2019 15:00:00 UTC. Similar to O2, calibration lines were injected into the control loop to measure time-dependent calibration parameters which track slowly-varying changes in the sensing and actuation transfer functions. We calculated z-scores of the coupled-cavity pole frequency f_{cc} and the optical gain κ_C, which track variations in the sensing function, as well as the actuation coefficients of the upper-intermediate, penultimate, and test-mass suspension stage actuators, κ_{UIM}, κ_{PUM}, and κ_{TST} respectively. During O3, the actuation functions of the upper-intermediate and penultimate suspension stages are being tracked separately with the parameters κ_{UIM} and κ_{PUM}, respectively. Thus, our expression for the time-dependence of the total actuation function is now

$$A(f,t) = \kappa_{UIM}(t)A_{UIM}(f,t_0) + \kappa_{PUM}(t)A_{PUM}(f,t_0) + \kappa_{TST}(t)A_{TST}(f,t_0) \qquad (6.1)$$

where $A_{UIM}(f,t_0)$, $A_{PUM}(f,t_0)$, and $A_{TST}(f,t_0)$, are the frequency-dependent actuation functions of the upper-intermediate, penultimate, and test-mass suspension stage actuators measured at reference time $t = t_0$.

The same analysis that was carried out on O2 data was carried out on O3a data. However, several times during the run, one or more time-dependent calibration parameter was artificially held at a constant value during time segments corresponding to high uncertainty in the calibration lines in order to maintain a best estimate for the time being, and many of those segments were long enough in duration to result in very large z-score magnitudes that would dominate the results. Thus, the algorithm was adjusted to ignore such segments when it encounters them, and the analysis was reran. Because of this, different percentages of the total O3a observational data were analyzed for each time-dependent calibration parameter; however, the differences were not vast. Taking into

account our omission of flat segments, padding around observational segments and padding around data quality veto segments, the analysis still covered the majority of O2 observational data. At LHO, approximately 74.7% of the total observational data was analyzed for f_{cc} and κ_C, 76.8% of the data for κ_{PUM}, 75.5% for κ_{UIM}, and 77.2% of the data for was analysed for κ_{TST}. At LLO, approximately 67.8% of the total observational data was analysed for f_{cc} and κ_C, 72.0% for κ_{UIM}, and approximately 72.5% of the data was analyzed for κ_{TST}.

Overall, the results show that all the time-dependent calibration parameters were well-behaved throughout O3a. Table 6.1 enumerates the number of noise transients out algorithm found using a minimum z-score magnitude of $|Z| \geq 5$. The following subsections will discuss the performance of each parameter in a bit more detail.

Table 6.1: Break down of the number of individual noise transients isolated by our algorithm using an $|z| \geq 5$ threshold for O3a. The first column lists the parameter symbols. The 2nd and 4th columns list the number of transients found by our method during O3a for LHO and LLO respectively. The 3rd and 5th columns list the percentage of the total O3a observational time for LHO and LLO respectively.

Parameter	No. at LHO	% of O3a (LHO)	No. at LLO	% of O3a (LLO)
f_{cc}	21	0.0038	42	0.0093
κ_C	34	0.0062	23	0.0033
$\kappa_{UIM}\}$	35	0.0065	91	0.0164
$\kappa_{PUM}\}$	40	0.0101	79	0.0216
κ_{TST}	47	0.0079	89	0.0210

Fig. 6.1 is a histogram of the f_{cc} z-score distributions using LHO data compared to the corresponding distribution using LLO data. The z-score results of f_{cc} at both detectors consistent with a Normal Gaussian distribution, with only the rare small excursion. At LHO, there were 21 noise transients found with a peak z-score magnitude greater than or equal to 5. The largest had a speak z-score magnitude of $|z| = 8.70$. Fig. 6.2 is a time series plot of 1024 seconds centered on the GPS time corresponding to the peak z-score of the highest-scoring f_{cc} noise transient at the LHO detector. Even though this event was the most significant transient found in the LHO coupled-cavity pole frequency, the measurement only deceased approximately 2 Hz for roughly 5
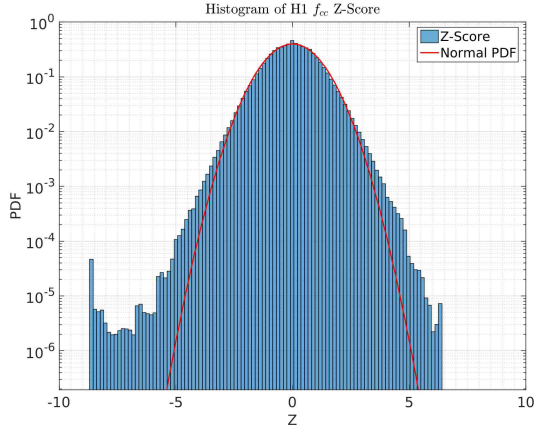
(a) f_{cc} z-score distribution of LHO O3a data.
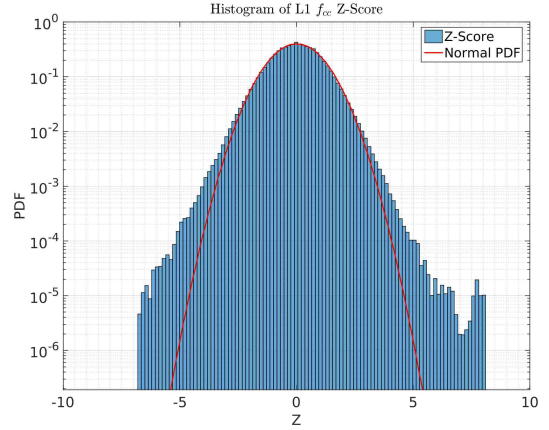
(b) f_{cc} z-score distribution of LLO O3a data.

Figure 6.1: Histograms of f_{cc} z-scores using O3a data from LHO *(left)* and LLO *(right)*. These plots show that for both detectors, the vast majority of data points fit within a Normal probability distribution function (red trace); however, these plots also show evidence of fast noise transients, especially at LLO.

minutes. That is very modest compared to the most significant transient in f_{cc} during O2, when the coupled-cavity pole dropped over 100 Hz (Figs. 5.8).
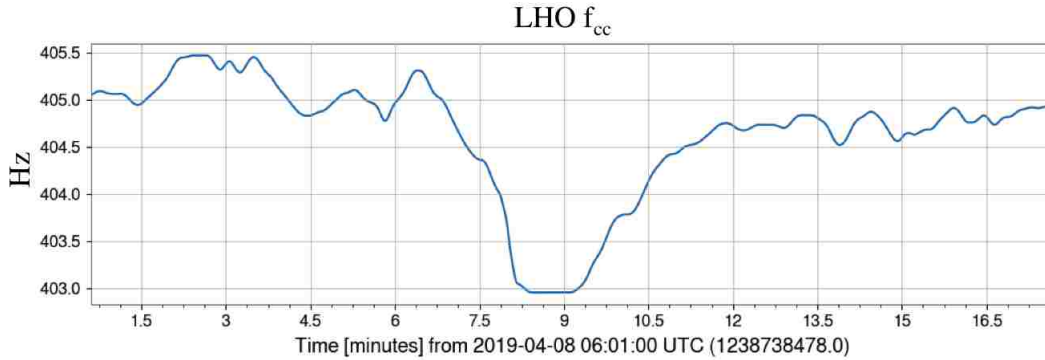

Figure 6.2: Time series of 1024 seconds centered on the transient in the LLO f_{cc} that had the highest peak z-score magnitude in O3a.

At LLO, the algorithm found 42 noise transients in f_{cc}, the largest had a peak z-score magnitude of only $|z| = 8.06$. Fig. 6.3 is a time series plot of 1024 seconds centered on the GPS time corresponding to the peak z-score of the highest-scoring f_{cc} noise transient at the LLO detector. Likewise, despite this being the most significant event found in the LLO coupled-cavity pole frequency, we see that it only increased approximately 4 Hz over a during of roughly 3 minutes, which again is not a cause for concern.
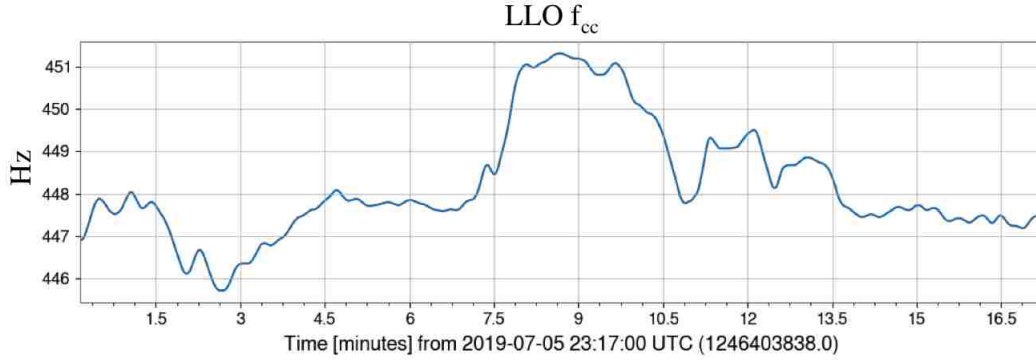
41

Figure 6.3: Time series of 1024 seconds centered on the transient in the LHO f_{cc} that had the highest peak z-score magnitude in O3a.
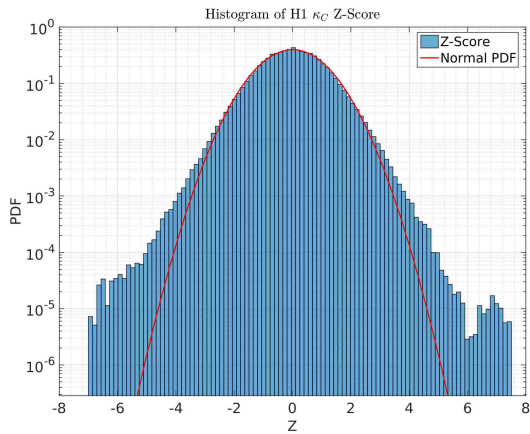
(a) κ_C z-score distribution of LHO O3a data.
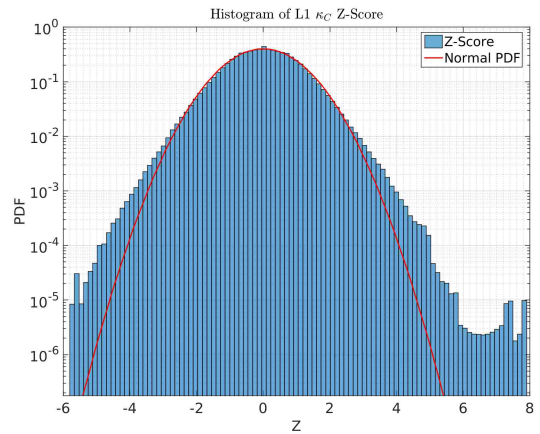
(b) κ_C z-score distribution of LLO O3a data.

Figure 6.4: Histograms of κ_C z-scores using O3a data from LHO *(left)* and LLO *(right)*. These plots show that for both detectors, the vast majority of data points fit within a Normal probability distribution function (red trace); however, these plots also show strong evidence of fast noise transients at both detectors.

Fig. 6.4 is a histogram of the κ_C z-score distributions using LHO data compared to the corresponding distribution using LLO data. The z-score results of at both detectors were consistent with a Normal Gaussian distribution, with only rare, small excursions. At LHO, we found 34 separate transients; the most significant of which had a very modest peak z-score magnitude of $|z| = 6.01$. Likewise at LLO, we found 23 transients, but the largest had a peak z-score magnitude of only $|z| = 7.89$. Overall, none of the transients found by our algorithm are large enough to cause significant detriment to the calibration.
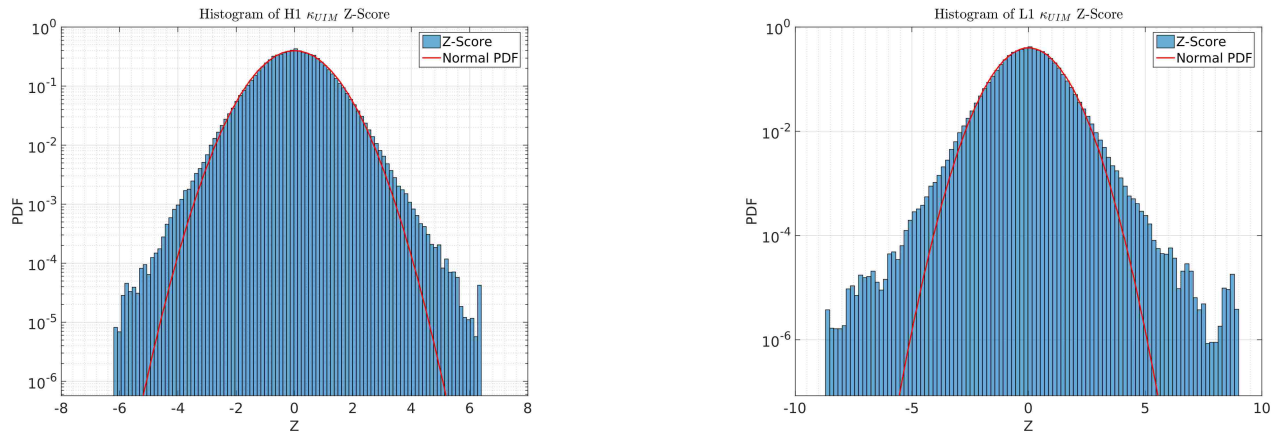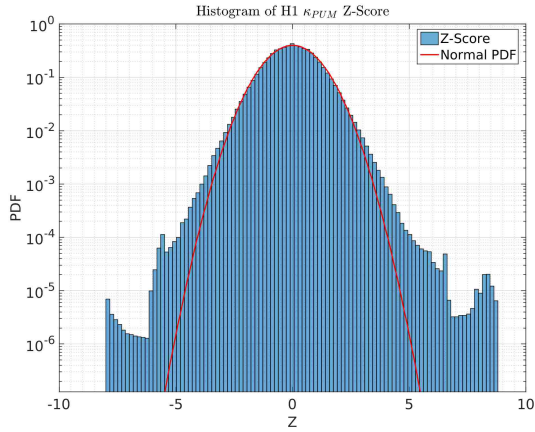

(a) κ_{UIM} z-score distribution of LHO O3a data.

(b) κ_{UIM} z-score distribution of LLO O3a data.

Figure 6.5: Histograms of κ_{UIM} z-scores using O3a data from LHO *(left)* and LLO *(right)*. These plots show that for both detectors, the vast majority of data points fit within a Normal probability distribution function (red trace); however, these plots show evidence of fast noise transients, especially at LLO.

Fig.6.5 compares the distributions of the z-scores of the upper-intermediate stage actuation coefficient κ_{UIM}. As usual, both are mostly consistent with a Normal Gaussian distribution. For LHO, the algorithm found 35 transient events, and the most significant transient had a peak z-score magnitude of $|z| = 6.37$. At LLO, there were 91 transients found, but again the most significant had a modest peak z-score magnitude of $|z| = 8.98$.

Fig.6.6 is the histogram comparison of the penultimate-stage actuation coefficient κ_{PUM}. The distribution at LHO is consistent with a Normal Gaussian with 40 transient identified by the algorithm. The most significant had a peak z-score magnitude of $|z| = 8.71$. On the other hand, while the LLO distribution is mostly consistent with a Normal Gaussian, it is indicative of the

(a) κ_{PUM} z-score distribution of LHO O3a data.

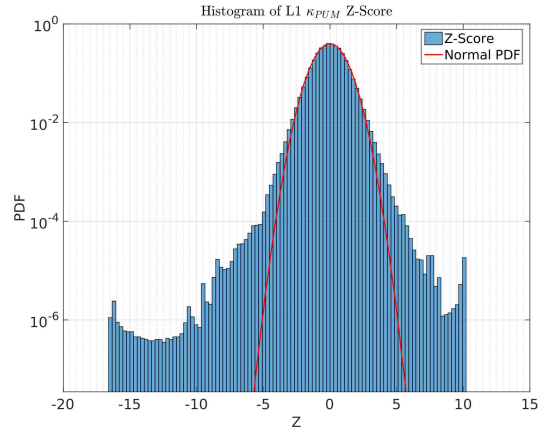(b) κ_{PUM} z-score distribution of LLO O3a data.

Figure 6.6: Histograms of κ_{PUM} z-scores using O3a data from LHO *(left)* and LLO *(right)*. These plots show that for both detectors, the vast majority of data points fit within a Normal probability distribution function (red trace); however, these plots show evidence of fast noise transients, especially at LLO.

possibility of a somewhat significant transient. Indeed the algorithm detected 79 transients, and the most significant had a peak z-score magnitude of $|z| = 16.47$, which is comparatively large. However, upon closer investigation it was found that unfortunately one long-duration flat segment made it into the analysis (Fig. 6.7), so this result has been omitted. Thus, the most significant valid transient had a peak z-score magnitude of $|z| = 10.19$, which is still fairly large compared to other results. Fig. 6.8 is a time series of 1024 seconds centered around the peak z-score of that transient, which shows only an increase of approximately 1.5% over roughly a 3-minute duration.
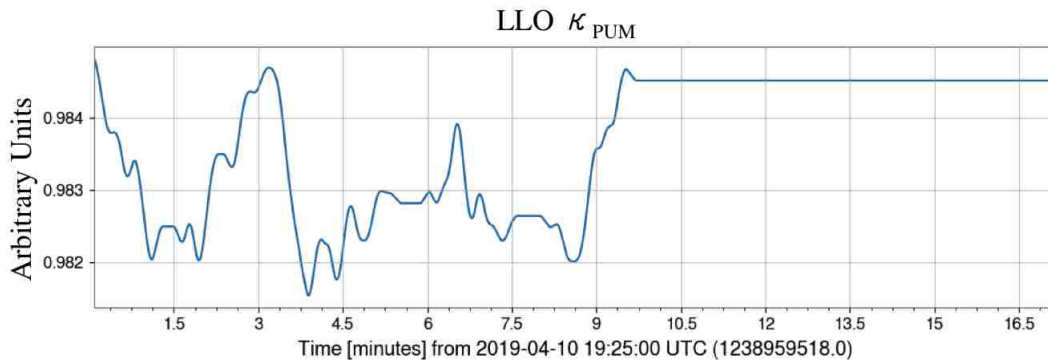

Figure 6.7: Time series of 1024 seconds centered on the transient in the LHL κ_{PUM} that had the highest peak z-score magnitude in O3a due to an erroneous segment of flat data.
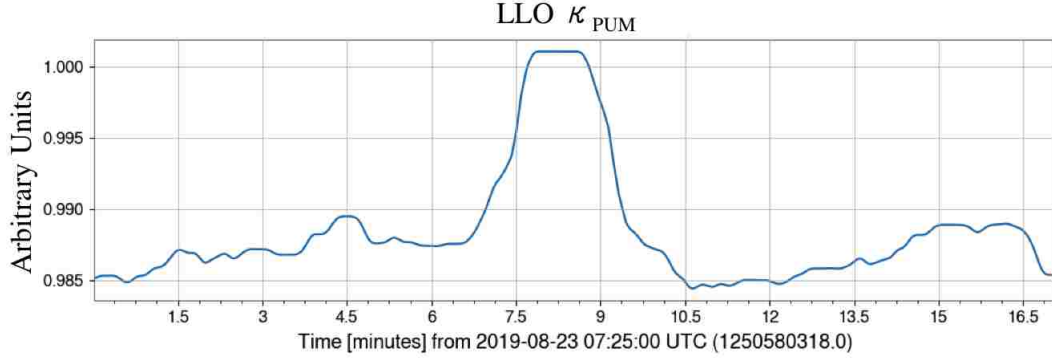
Figure 6.8: Time series of 1024 seconds centered on the transient in the LHO κ_{PUM} that had the highest valid peak z-score magnitude in O3a.
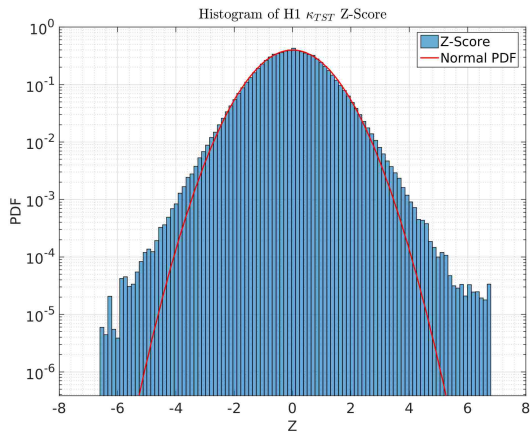
(a) κ_{PUM} z-score distribution of LHO O3a data.
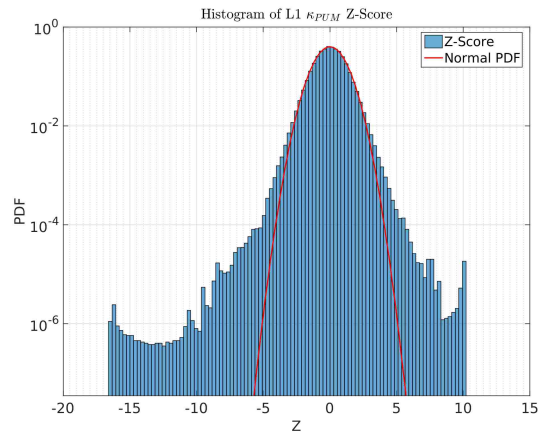
(b) κ_{PUM} z-score distribution of LLO O3a data.

Figure 6.9: Histograms of κ_{PUM} z-scores using O3a data from LHO *(left)* and LLO *(right)*. These plots show that for both detectors, the vast majority of data points fit within a Normal probability distribution function (red trace); however, these plots show evidence of fast noise transients, especially at LLO.

Fig.6.9 is the histogram comparison of the test-mass-stage actuation coefficient κ_{TST} at both detectors. The LHO distribution is mostly consistent with a Normal Gaussian with only small, rare excursions. However, the LLO histogram shows evidence of a moderately large transient. For LHO, we found 47 transients, and the largest had a peak z-score magnitude of $|z| = 6.78$, which is not significant enough for alarm. On the other hand, scanning LLO data resulted in 89 transients, the largest of which having a peak z-score magnitude of $|z| = 22.5$, which would be cause for alarm; however, this is the second and last instance of a long-duration flat segment unfortunately making its way into the analysis (Fig. 6.10). Thus, this transient was omitted as well. Fig. 6.11 is a time series of the highest-scoring remaining transient, which corresponded to a peak z-score magnitude of $|z| = 10.52$. Despite the moderately large score, the parameter is seen to increase only approximately 1.1% for roughly 3 minutes.

Figure 6.10: Time series of 1024 seconds centered on the transient in the LHO κ_{TST} that had the highest peak z-score magnitude in O3a due to an erroneous segment of flat data.

6.2. Conclusions

This analysis demonstrates that the time-dependent calibration tracking system operated with good fidelity during O3a. No serious transients were found in the LHO or LLO calibration parameters.
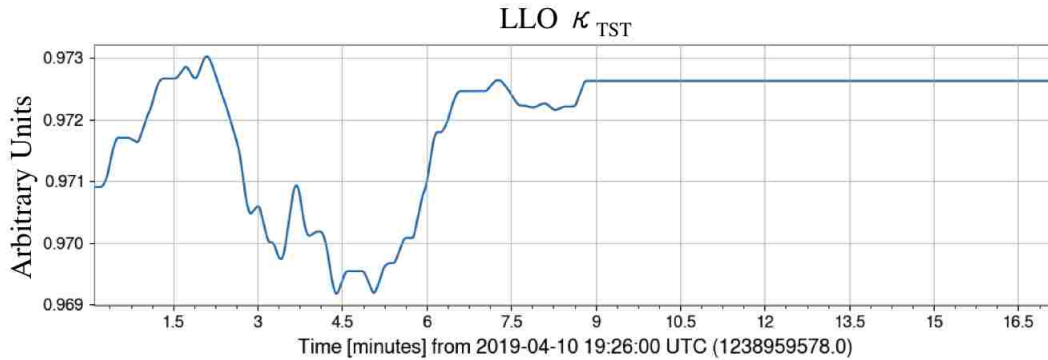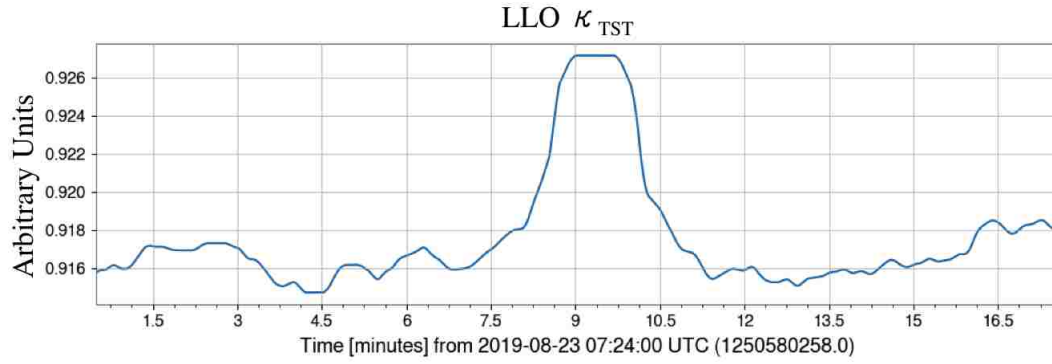
Figure 6.11: Time series of 1024 seconds centered on the transient in the LHO κ_{TST} that had the highest valid peak z-score magnitude in O3a.

CHAPTER 7. CONCLUSIONS

Our work in the LIGO photon calibrator project was able to design and implement a method of estimating the photon beam spot locations on the end-station test masses that was minimally invasive, requiring no venting of the vacuum chambers or any significant interaction with the core optics or other contents of the vacuum chamber which are held under strict contamination standards. This new method used in-air cameras which took photographs of the test masses through a view-port on the end-station vacuum chambers, and the beam spot locations were estimated by using the photographs to construct a basis transformation between the photograph and the test mass surface. We determined that the offsets of the beam positions from the nominal locations would contribute to an uncertainty in the photon calibrator displacement of approximately 0.1%, which is negligible compared to displacement uncertainties introduced by bulk elastic deformations on the surface of the test mass. Furthermore, this method allowed for intermittent estimations to be carried out throughout observation runs which demonstrated that the photon calibrator beam spots were not subject to significant drifts over the time scales of an observation run.

In addition, we present a novel method of detecting and characterizing large fluctuations in the LIGO time-dependent calibration parameters. Our method is able to compensate for the slowly-varying non-stationarity of the calibration parameters by applying a swept time-window through the data to calculate and associated value that demonstrates the statistical significance of each data point against a standardized background based on the behavior of the data within the temporal neighborhood of the datum in question. This method has not been previously used to analyze the LIGO time-dependent calibration parameters. Furthermore, the results of our work demonstrated that fluctuations in the optomechanical response of both LIGO interferometers were accurately compensated for in the time-dependent calibration model. The z-scores were largely consistent with Normal-Gaussian random data. In all the parameters, the noise transients were rare, and in all but the coupled-cavity pole frequency f_{cc} and optical gain κ_C at LLO, all of the transients that

we found with our method were small enough to have a negligible impact on strain reconstruction. The z-scores of the O3a time-dependent calibration parameters likewise were largely consistent with Normal-Gaussian random noise, and did not indicate any transients that would cause significant detriment to gravitational-wave measurements. The most significant transients found in our entire analysis of both O2 and O3a were occurred during O2 in f_{cc} and κ_C at LLO, and only corresponded to a increase in calibration uncertainty from 1.2% to 3.4% in the regime of the interfermeters' most sensitive frequency band (150 Hz).

REFERENCES

[1] TJ Aasi et al. Advanced ligo. *Classical and Quantum Gravity*, 32(7):074001, 2015. URL `http://stacks.iop.org/0264-9381/32/i=7/a=074001`.

[2] B. P. Abbott et al. Observation of gravitational waves from a binary black hole merger. *Phys. Rev. Lett.*, 116:061102, Feb 2016. doi: 10.1103/PhysRevLett.116.061102. URL `https://link.aps.org/doi/10.1103/PhysRevLett.116.061102`.

[3] B. P. Abbott et al. Multi-messenger observations of a binary neutron star merger. *The Astrophysical Journal*, 848(2):L12, oct 2017. doi: 10.3847/2041-8213/aa91c9. URL `https://doi.org/10.3847%2F2041-8213%2Faa91c9`.

[4] B. P. Abbott et al. Gw170817: Observation of gravitational waves from a binary neutron star inspiral. *Phys. Rev. Lett.*, 119:161101, Oct 2017. doi: 10.1103/PhysRevLett.119.161101. URL `https://link.aps.org/doi/10.1103/PhysRevLett.119.161101`.

[5] Sean M. Carroll. *Spacetime and geometry: An introduction to general relativity*. 2004. ISBN 0805387323, 9780805387322. URL `http://www.slac.stanford.edu/spires/find/books/www?cl=QC6:C37:2004`.

[6] P.R. Saulson. *Fundamentals of Interferometric Gravitational Wave Detectors*. World Scientific, 1994. ISBN 9789810218201. URL `https://books.google.com/books?id=4JyGQgAACAAJ`.

[7] K. Riles. Gravitational Waves: Sources, Detectors and Searches. *Prog. Part. Nucl. Phys.*, 68: 1–54, 2013. doi: 10.1016/j.ppnp.2012.08.001.

[8] Xavier Siemens, Bruce Allen, Jolien Creighton, Martin Hewitson, and Michael Landry. Making h (t) for ligo. *Classical and Quantum Gravity*, 21(20):S1723, 2004. URL `http://stacks.iop.org/0264-9381/21/i=20/a=015`.

[9] D Tuyenbayev, S Karki, J Betzwieser, C Cahillane, E Goetz, K Izumi, S Kandhasamy, J S Kissel, G Mendell, M Wade, A J Weinstein, and R L Savage. Improving ligo calibration accuracy by tracking and compensating for slow temporal variations. *Classical and Quantum Gravity*, 34(1):015002, 2017. URL `http://stacks.iop.org/0264-9381/34/i=1/a=015002`.

[10] L Carbone, S M Aston, R M Cutler, A Freise, J Greenhalgh, J Heefner, D Hoyland, N A Lockerbie, D Lodhia, N A Robertson, C C Speake, K A Strain, and A Vecchio. Sensors and actuators for the advanced ligo mirror suspensions. *Classical and Quantum Gravity*, 29(11): 115005, 2012. URL `http://stacks.iop.org/0264-9381/29/i=11/a=115005`.

[11] Evan D Hall, Craig Cahillane, Kiwamu Izumi, Rory J E Smith, and Rana X Adhikari. Systematic calibration error requirements for gravitational-wave detectors via the cramrrao

bound. *Classical and Quantum Gravity*, 36(20):205006, Sep 2019. ISSN 1361-6382. doi: 10.1088/1361-6382/ab368c. URL `http://dx.doi.org/10.1088/1361-6382/ab368c`.

[12] S. Karki, D. Tuyenbayev, S. Kandhasamy, B. P. Abbott, T. D. Abbott, E. H. Anders, J. Berliner, J. Betzwieser, C. Cahillane, L. Canete, C. Conley, H. P. Daveloza, N. De Lillo, J. R. Gleason, E. Goetz, K. Izumi, J. S. Kissel, G. Mendell, V. Quetschke, M. Rodruck, S. Sachdev, T. Sadecki, P. B. Schwinberg, A. Sottile, M. Wade, A. J. Weinstein, M. West, and R. L. Savage. The advanced ligo photon calibrators. *Review of Scientific Instruments*, 87(11): 114503, 2016. doi: 10.1063/1.4967303. URL `https://doi.org/10.1063/1.4967303`.

[13] H P Daveloza, M Afrin Badhan, M Diaz, K Kawabe, P N Konverski, M Landry, and R L Savage. Controlling calibration errors in gravitational-wave detectors by precise location of calibration forces. *Journal of Physics: Conference Series*, 363:012007, jun 2012. doi: 10. 1088/1742-6596/363/1/012007. URL `https://doi.org/10.1088%2F1742-6596%2F363%2F1%2F012007`.

[14] Craig Cahillane, Joe Betzwieser, Duncan A. Brown, Evan Goetz, Evan D. Hall, Kiwamu Izumi, Shivaraj Kandhasamy, Sudarshan Karki, Jeff S. Kissel, Greg Mendell, Richard L. Savage, Darkhan Tuyenbayev, Alex Urban, Aaron Viets, Madeline Wade, and Alan J. Weinstein. Calibration uncertainty for advanced ligo's first and second observing runs. *Phys. Rev. D*, 96: 102001, Nov 2017. doi: 10.1103/PhysRevD.96.102001. URL `https://link.aps.org/doi/10.1103/PhysRevD.96.102001`.

VITA

Thomas Abbott grew up in Chino, California. He went to high school at Don Antonio Lugo High School. He studied physics at California State University, Fullerton where he earned a B.S. in physics in 2010 and a M.S. in physics in 2012. In the summer of 2012 he moved to Baton Rouge, Louisiana to enroll in the physics Ph.D. program at Louisiana State University, from which he plans to graduate in May 2020.